Numerical simulation of tsunami waves generated by deformable submarine landslides

Gangfeng Ma [a],[*], James T. Kirby [b], Fengyan Shi [b]

[a] Department of Civil and Environmental Engineering, Old Dominion University, Norfolk, VA, USA
[b] Center for Applied Coastal Research, University of Delaware, Newark, DE 19716, USA

ABSTRACT

This paper presents a new submarine landslide model based on the non-hydrostatic wave model NHWAVE of Ma et al. (2012). The landslide is modeled as a water–sediment mixture. The dense plume is driven by baroclinic pressure forcing introduced by spatial density variations. The model is validated using laboratory measurements of turbidity currents and of water wave generation by a granular landslide. The model is then utilized to study the dependence of landslide motion and associated tsunami wave generation on parameters including sediment settling velocity, initial depth of the landslide and slide density. Model results show that the slide motion and water waves which it generates are both sensitive to these parameters. The relative tsunamigenic response to rigid and deformable landslides of equal initial geometry and density is also examined. It is found that the wave energy is mostly concentrated on a narrow band of the dominant slide direction for the waves generated by rigid landslides, while directional spreading is more significant for waves generated by deformable landslides. The deformable landslide has larger speed and acceleration at the early stage of landslide, resulting in larger surface waves. The numerical results indicate that the model is capable of reasonably simulating tsunami wave generation by submarine landslides.

Published by Elsevier Ltd.

1. Introduction

Landslides, or submarine mass failures (SMFs), are presently thought to be one of the major mechanisms for tsunami generation in coastal areas (Masson et al., 2006). Owing to the large volume involved, landslides can generate very large and energetic surface waves (Abadie et al., 2012), producing high wave run-up along the coast. For example, submarine mass failure is considered as one of the major sources for the 1998 Papua New Guinea tsunami that caused great loss in human life (Synolakis et al., 2002; Tappin et al., 2001, 2002). Compared to seismogenic tsunami, landslide induced tsunami waves feature relatively shorter wavelengths, and hence frequency dispersion effects can be significant or even dominant in the wave evolution process. Interactions between the landslide and the associated waves are strong and will affect the characteristics of both (Jiang and Leblond, 1992; Assier-Rzadkie-wicz et al., 1997). Numerical simulation of landslide tsunamis has to take these factors into consideration.

Tremendous effort has been devoted to simulating landslide tsunami generation in the last several decades. Various computational models have been employed using different levels of simplification; for example, shallow water theory (Harbitz, 1992), fully nonlinear potential flow (Grilli and Watts, 1999, 2005; Grilli et al., 2002), Boussinesq equations (Lynett and Liu, 2003; Watts et al., 2003; Fuhrman and Madsen, 2009; Zhou and Teng, 2010), non-hydrostatic wave equations (Ma et al., 2012) and Navier–Stokes equations (Heinrich, 1992; Liu et al., 2005; Yuk et al., 2006; Ataie-Ashtiani and Shobeyri, 2008; Abadie et al., 2010; Montagna et al., 2011; Horrilo Horrillo et al. (2013)). Most of these models treat the landslide as a rigid solid with prescribed slide shape and behavior. The slide motion, which is generally accounted for through a moving boundary condition, is specified based on a dynamic force balance on the sliding mass involving weight, buoyancy, friction, hydrodynamic drag and inertia forces (Enet Grilli and Watts, 2005). An exception is the model of Abadie et al. (2010), in which the coupling between the rigid slide and water is implicitly computed, rather than specifying known slide kinematics. All of these models are able to accurately reproduce water waves generated by rigid sliding objects as observed in the laboratory environment. As summarized by Abadie et al. (2010, 2012), however, the methodology employed in these models has severe limitations in application to real cases, where landslides are always deformable. Due to its time-varying 3D geometry, rheology as well as slide–water interactions, the deformable landslide is much more complex than a rigid slide. It is impossible to prescribe slide kinematics a priori. In this sense, more advanced

* Corresponding author. Tel.: +1 757 683 4732.
E-mail address: gma@odu.edu (G. Ma).

models are needed, which allow the slide to deform and are capable of describing the two-way coupling between the slide and surrounding water (Jiang and Leblond, 1992, 1993; Abadie et al., 2012).

Attempts have been made to develop more sophisticated numerical models for deformable landslides. Most of the existing deformable models were based on long-wave approximation. The landslides were modeled as either rheological materials or granular flow. For example, Jiang and Leblond (1992, 1993) developed a model to study the coupling between a deformable submarine landslide and associated tsunami waves based on the assumption that the slide material is not diluted while flowing downslope. The long-wave approximation was adopted for both water waves and the landslide. The slide flow was assumed to be laminar with a parabolic distribution of the horizontal velocity. They applied the model to study the wave characteristics and the parameters dominating the slide-wave interactions. Their model is able to capture the slide motion and tsunami wave generation. Imran et al. (2001) proposed a 1D two-layer numerical model (BING1D) describing the downslope development of submarine debris flows. Their model incorporates three rheological models as user defined alternatives. Similar to Jiang and Leblond (1993), the long wave approximation is adopted and the flow is assumed to remain laminar throughout the computation. Watts and Grilli (2003) employed the BING model to study the underwater landslide shape, motion and deformation at early times. Recently, Kelfoun and Druitt (2005), Kelfoun et al. (2010) and Giachetti et al. (2011) developed a depth-averaged granular flow model, which was coupled with a shallow water flow model to simulate tsunamis generated by large debris avalanches. The long-wave approximation has intrinsic limitations which prevent these models from being applied to most submarine landslides where vertical accelerations and frequency dispersion are not negligible. To avoid the long-wave assumption, Navier–Stokes solvers with advanced free surface capturing schemes such as the Volume-of-Fluid (VOF) method and smoothed particle hydrodynamics (SPH) approach have been proposed to simulate tsunami wave generation by deformable landslides. Assier-Rzad-kiewicz et al. (1997) proposed a 2D sediment–water mixture model for submarine landslides based on Navier–Stokes equations. In their model, the free surface motion was captured by a volume of fluid (VOF) approach. The dense part was considered as a Bingham fluid, and the dispersed part was modeled as an ideal fluid. The model was applied to simulate a laboratory landslide. The results showed that the model could reproduce the water waves generated by the landslide in reasonable accuracy. Ataie-Ashtiani and Shobeyri (2008) developed a similar model using meshless smoothed particle hydrodynamics (SPH) method. Their model could also predict landslide-induced wave generation by adjusting the rheology of the mud. These models have not been applied to simulate marine landslides at large scales, which are different from the landslides at laboratory scales. Abadie et al. (2012) employed a 3D multi-fluid Navier–Stokes model THETIS to simulate tsunami waves generated by the potential collapse of the west flank of the Cumbre Vieja Volcano (CVV), Canary Island, Spain. The free surface and slide–water interface were captured by the VOF algorithm. The deformable landslide was considered as an inviscid fluid with a constant density. The model was successfully applied to study CVV tsunami generation. Horrillo et al. (2013) developed a simplified 3D Navier–Stokes model for full scale landslide scenario in the Gulf of Mexico, the East-Breaks underwater landslide. Their model used a simplified and relatively diffusive free surface capturing scheme to speed up the simulations.

During submarine landslides, strong free surface deformation, large vertical acceleration and non-hydrostatic pressure may occur. As discussed by Abadie et al. (2012), these phenomena may significantly affect energy transfer between slide and surrounding

water, and can only be modeled by 3D Navier–Stokes models. The Navier–Stokes solvers discussed above use either VOF algorithm or SPH method to simulate free surface, which are computationally expensive. This paper describes a new submarine landslide model based on a Non-Hydrostatic WAVE model (NHWAVE). The slide is considered as water–sediment mixture, which can be diffused and diluted during its movement. The dense plume is driven by the baroclinic pressure forcing, which is introduced by the spatial density variation. The current model is anticipated to be able to better represent the deformable landslide than that of Abadie et al. (2012), in which the submarine landslide was modeled as inviscid dense fluid.

The present landslide model is still a simplified one as the particle–particle interactions are not considered. The inter-particulate stresses may slow down the slide motion. These processes will be implemented in the future. Comparing with the existing landslide models based on VOF or SPH approaches, another major advantage of the current model is the computational efficiency because (1) less vertical layers are required to capture the landslide motion and (2) free surface is directly solved. Therefore, the current model is practically feasible for modeling 3D large-scale submarine mass failure in the ocean.

The paper is organized as follows. Section 2 introduces the model formulations and numerical scheme. Section 3 presents the model validation using laboratory measurements on turbidity currents. Section 4 applies the model to study tsunami waves generated by landslides at both laboratory and large scales. Section 5 gives the conclusions of the paper.

2. Formulation

The model we employed in this study is the Non-Hydrostatic WAVE model NHWAVE, which was recently developed by Ma et al. (2012) to study the propagation of fully dispersive, fully nonlinear surface waves in complex 3D coastal environments as well as tsunami wave generation by a prescribed bottom motion. NHWAVE solves the incompressible Navier–Stokes equations in well-balanced conservative form, formulated in time-dependent, surface and terrain-following σ coordinates. The governing equations are discretized by a combined finite volume/finite difference approach with a Godunov-type shock-capturing scheme. The model is wave-resolving and can provide instantaneous descriptions of surface displacement and wave orbital velocities. In this section, we discuss recent extensions to the model to enable the study of tsunami wave generation by deformable landslides.

2.1. Governing equations

Submarine landslides are commonly induced by the liquefaction of sediment, which may generate highly turbid currents near the bottom. The sediment concentration in the turbidity currents is so high that it is necessary to simulate sediment transport and water flow in a coupled way. From the macroscopic point of view, the presence of sediment in the water column not only changes the density of the mixture, but also affects the turbulent velocity fluctuations. In this study, the sediment-sediment interactions are neglected for simplicity. The turbidity flow is considered as a mixture of water and sediment, with the mixture density ρ_m defined as

$$\rho_m = (1 - C)\rho_0 + C\rho_s \tag{1}$$

where C is the sediment volume concentration, $\rho_0 = 1000 \text{ kg/m}^3$ is the density of water, and $\rho_s = 2650 \text{ kg/m}^3$ is the density of sediment.

A surface and terrain-following σ coordinate is adopted to transform the governing equations, given by

$$t = t^*, \quad x = x^*, \quad y = y^*, \quad \sigma = \frac{z^* + h}{D} \tag{2}$$

where (x^*, y^*, z^*) is the Cartesian coordinate system. $D = h + \eta$ is the total water depth, h is the still water depth, and η is the surface displacement.

With the sediment effects, the continuity and momentum equations in well-balanced conservative form (Fuhrman and Madsen, 2009; Fuhrman and Madsen, 2009; Lai et al., 2010) are written as

$$\frac{\partial D}{\partial t} + \frac{\partial Du}{\partial x} + \frac{\partial Dv}{\partial y} + \frac{\partial \omega}{\partial \sigma} = 0 \tag{3}$$

$$\frac{\partial \mathbf{U}}{\partial t} + \frac{\partial \mathbf{F}}{\partial x} + \frac{\partial \mathbf{G}}{\partial y} + \frac{\partial \mathbf{H}}{\partial \sigma} = \mathbf{S}_h + \mathbf{S}_p + \mathbf{S}_\rho + \mathbf{S}_\tau \tag{4}$$

in which $\mathbf{U} = (Du, Dv, Dw)^T$, (u, v, w) are velocities in Cartesian coordinates. ω is the vertical velocity in σ coordinates, defined by

$$\omega = D\left(\frac{\partial \sigma}{\partial t^*} + u\frac{\partial \sigma}{\partial x^*} + v\frac{\partial \sigma}{\partial y^*} + w\frac{\partial \sigma}{\partial z^*}\right) \tag{5}$$

with

$$\begin{aligned}
\frac{\partial \sigma}{\partial t^*} &= -\frac{\sigma}{D}\frac{\partial D}{\partial t} \\
\frac{\partial \sigma}{\partial x^*} &= \frac{1}{D}\frac{\partial h}{\partial x} - \frac{\sigma}{D}\frac{\partial D}{\partial x} \\
\frac{\partial \sigma}{\partial y^*} &= \frac{1}{D}\frac{\partial h}{\partial y} - \frac{\sigma}{D}\frac{\partial D}{\partial y} \\
\frac{\partial \sigma}{\partial z^*} &= \frac{1}{D}
\end{aligned} \tag{6}$$

The fluxes in Eq. (4) are given by

$$\mathbf{F} = \begin{pmatrix} Duu + \frac{1}{2}g\eta^2 + gh\eta \\ Duv \\ Duw \end{pmatrix}, \quad \mathbf{G} = \begin{pmatrix} Duv \\ Dvv + \frac{1}{2}g\eta^2 + gh\eta \\ Dvw \end{pmatrix}, \quad \mathbf{H} = \begin{pmatrix} u\omega \\ v\omega \\ w\omega \end{pmatrix}$$

The source terms $\mathbf{S}_h$, $\mathbf{S}_p$, $\mathbf{S}_\tau$ are related to hydrostatic pressure, non-hydrostatic pressure and turbulent diffusion, respectively,

$$\mathbf{S}_h = \begin{pmatrix} g\eta\frac{\partial h}{\partial x} \\ g\eta\frac{\partial h}{\partial y} \\ 0 \end{pmatrix}, \quad \mathbf{S}_p = \begin{pmatrix} -\frac{D}{\rho}\left(\frac{\partial p}{\partial x} + \frac{\partial p}{\partial \sigma}\frac{\partial \sigma}{\partial x^*}\right) \\ -\frac{D}{\rho}\left(\frac{\partial p}{\partial y} + \frac{\partial p}{\partial \sigma}\frac{\partial \sigma}{\partial y^*}\right) \\ -\frac{1}{\rho}\frac{\partial p}{\partial \sigma} \end{pmatrix}, \quad \mathbf{S}_\tau = \begin{pmatrix} DS_{\tau_x} \\ DS_{\tau_y} \\ DS_{\tau_z} \end{pmatrix}$$

where $DS_{\tau_x}, DS_{\tau_y}, DS_{\tau_z}$ are diffusion terms, p is the dynamic pressure.

Another source term $\mathbf{S}_\rho$ is induced by horizontal density gradient, known as the baroclinic pressure forcing. The mixture density ρ_m can be expressed as $\rho_0 + \rho$, where ρ_0 is the constant reference density taken as the water density in this study, and the residual $\rho = \rho_m - \rho_0 = C(\rho_s - \rho_0)$. The hydrostatic pressure is thus defined by

$$\frac{\partial p_h}{\partial z} = -(\rho_0 + \rho)g \tag{7}$$

The horizontal hydrostatic pressure gradient is then given by

$$\frac{1}{\rho_0}\nabla p_h = g\nabla \eta + g\nabla r \tag{8}$$

where r is the baroclinic pressure head.

$$r = \frac{1}{\rho_0}\int_z^\eta \rho \, dz \tag{9}$$

Thus, the baroclinic source term is given by $\mathbf{S}_\rho = -gD\nabla r$ in z coordinate.

2.2. Sediment transport model

The suspended sediment concentration can be computed from the convection–diffusion equation for suspended sediment load, which is given as follows in σ coordinate.

$$\begin{aligned}
&\frac{\partial DC}{\partial t} + \frac{\partial DuC}{\partial x} + \frac{\partial DvC}{\partial y} + \frac{\partial(\omega - w_s)C}{\partial \sigma} \\
&= \frac{\partial}{\partial x}\left[D\left(v + \frac{v_t}{\sigma_h}\right)\frac{\partial C}{\partial x}\right] + \frac{\partial}{\partial y}\left[D\left(v + \frac{v_t}{\sigma_h}\right)\frac{\partial C}{\partial y}\right] \\
&\quad + \frac{1}{D}\frac{\partial}{\partial \sigma}\left[\left(v + \frac{v_t}{\sigma_v}\right)\frac{\partial C}{\partial \sigma}\right]
\end{aligned} \tag{10}$$

where C is the concentration of suspended sediment and w_s is sediment settling velocity. In the following, we will vary the sediment settling velocity to study its effects on landslide motion and associated tsunami waves. σ_h and σ_v are horizontal and vertical Schmidt numbers for sediment, respectively.

To solve the above equation, boundary conditions are needed to be specified at all the physical boundaries. Specifically, at the free surface, the vertical sediment flux is zero. At the bed-fluid interface, there is mass exchange of suspended sediment, which accounts for sediment erosion and deposition. However, in the following studies of submarine landslide, we assume that the submarine landslide is a self-sustained system. Thus, no mass exchange occurs at the bed. Therefore, a zero vertical flux boundary condition is imposed at both free surface and bottom.

$$\left(v + \frac{v_t}{\sigma_v}\right)\frac{1}{D}\frac{\partial C}{\partial \sigma} + w_s C = 0 \tag{11}$$

2.3. Turbulence model

We have implemented a nonlinear $k-\epsilon$ model (Lin and Liu, 1998a,b; Ma et al., 2011) into NHWAVE to simulate turbulent flow. The turbulent eddy viscosity is calculated by

$$v_t = C_\mu \frac{k^2}{\epsilon} \tag{12}$$

With sediment induced stratification effects, the $k-\epsilon$ equations in conservative form are given by

$$\frac{\partial Dk}{\partial t} + \nabla \cdot (D\mathbf{u}k) = \nabla \cdot \left[D\left(v + \frac{v_t}{\sigma_k}\right)\nabla k\right] + D(P_s + P_b - \epsilon) \tag{13}$$

$$\begin{aligned}
\frac{\partial D\epsilon}{\partial t} + \nabla \cdot (D\mathbf{u}\epsilon) &= \nabla \cdot \left[D\left(v + \frac{v_t}{\sigma_\epsilon}\right)\nabla \epsilon\right] \\
&\quad + \frac{\epsilon}{k}D(C_{1\epsilon}(P_s + C_{3\epsilon}P_b) - C_{2\epsilon}\epsilon)
\end{aligned} \tag{14}$$

where σ_k, σ_ϵ, $C_{1\epsilon}$, $C_{2\epsilon}$, C_μ are empirical coefficients (Rodi, 1987) given by

$$\begin{aligned}
\sigma_k &= 1.0, \quad \sigma_\epsilon = 1.3, \quad C_{1\epsilon} = 1.44, \\
C_{2\epsilon} &= 1.92, \quad C_\mu = 0.09
\end{aligned} \tag{15}$$

P_s and P_b are shear and buoyancy production, which are described as

$$P_s = -\overline{u_i' u_j'}\frac{\partial u_i}{\partial x_j^*} \tag{16}$$

and

$$P_b = \frac{g}{\rho_0}\frac{v_t}{D}\frac{\partial \rho_m}{\partial \sigma} \tag{17}$$

where the Reynolds stress $\overline{u_i' u_j'}$ is calculated by a nonlinear model proposed by Lin and Liu (1998a,b), which is given by

$$\overline{u_i' u_j'} = -C_d \frac{k^2}{\epsilon}\left(\frac{\partial u_i}{\partial x_j^*} + \frac{\partial u_j}{\partial x_i^*}\right) + \frac{2}{3}k\delta_{ij}$$

$$-C_1 \frac{k^3}{\epsilon^2}\left(\frac{\partial u_i}{\partial x_l^*}\frac{\partial u_l}{\partial x_j^*} + \frac{\partial u_j}{\partial x_l^*}\frac{\partial u_l}{\partial x_i^*} - \frac{2}{3}\frac{\partial u_l}{\partial x_k^*}\frac{\partial u_k}{\partial x_l^*}\delta_{ij}\right)$$

$$-C_2 \frac{k^3}{\epsilon^2}\left(\frac{\partial u_i}{\partial x_k^*}\frac{\partial u_j}{\partial x_k^*} - \frac{1}{3}\frac{\partial u_l}{\partial x_k^*}\frac{\partial u_l}{\partial x_k^*}\delta_{ij}\right)$$

$$-C_3 \frac{k^3}{\epsilon^2}\left(\frac{\partial u_k}{\partial x_i^*}\frac{\partial u_k}{\partial x_j^*} - \frac{1}{3}\frac{\partial u_l}{\partial x_k^*}\frac{\partial u_l}{\partial x_k^*}\delta_{ij}\right) \quad (18)$$

where C_d, C_1, C_2 and C_3 are empirical coefficients as given by Lin and Liu (1998a,b)

$$C_d = \frac{2}{3}\left(\frac{1}{7.4 + 2S_{\max}}\right), \quad C_1 = \frac{1}{185.2 + 3D_{\max}^2}$$

$$C_2 = -\frac{1}{58.5 + 2D_{\max}^2}, \quad C_3 = \frac{1}{370.4 + 3D_{\max}^2} \quad (19)$$

where

$$S_{\max} = \frac{k}{\epsilon}\max\left\{\left|\frac{\partial u_i}{\partial x_i^*}\right|\right\} \text{ (indices not summed)}$$

$$D_{\max} = \frac{k}{\epsilon}\max\left\{\left|\frac{\partial u_i}{\partial x_j^*}\right|\right\} \quad (20)$$

The above coefficients may ensure the non-negativity of turbulent velocities and bounded Reynolds stress. They have been successfully applied to simulate breaking waves on plane beaches (Lin and Liu, 1998a,b). Previous studies (Torres-Freyermuth and Hsu, 2010; Snyder and Hsu, 2011) have shown that sediment induced density stratification plays a critical role in damping the flow turbulence, and numerical results are very sensitive to the value of $C_{3\epsilon}$. They found that the value for stable stratification ($C_{3\epsilon} = 0.0$) gives the best comparison with laboratory measurements. Therefore, we use $C_{3\epsilon} = 0.0$ in the following studies.

2.4. Numerical scheme

A combined finite-volume and finite-difference scheme with a Godunov-type method is applied to discretize Eqs. (3) and (4) (Ma et al., 2012). In order to apply Godunov-type scheme, all the variables are defined at the cell centers except that dynamic pressure p is defined at the vertically-facing cell faces. The momentum equations are solved by a second-order Godunov-type finite volume method. The HLL approximate Riemann solver (Harten et al., 1983) is used to estimate fluxes at the cell faces, which has widely been proved to be robust and efficient (Shi et al., 2012; Ma et al., 2012). For the sediment transport equation and $k-\epsilon$ equations, the convective fluxes are determined using the hybrid linear/parabolic approximation (HLPA) scheme (Zhu, 1991), which has approximately second-order accuracy in space. To obtain second-order temporal accuracy, the two-stage second-order nonlinear Strong Stability-Preserving (SSP) Runge–Kutta scheme (Gottlieb et al., 2001) was adopted for adaptive time stepping. Uniform gridding is used in the horizontal direction while gridding in the vertical direction is generalized to be non-uniform in order to capture the bottom and surface boundary layers when desired. The Poisson equation for the pressure field, described in Ma et al. (2012), is discretized by the finite-difference method, resulting in an asymmetric coefficient matrix with a total of 15 diagonal lines. The linear system is solved using the high performance preconditioner HYPRE software library. The model is fully parallelized using Message Passing Interface (MPI) with non-blocking communication. Further details of the numerical method may be found in Ma et al. (2012).

To reduce the numerical diffusion of the model, a modification of HLL scheme called HLLC approximate Riemann solver proposed by Toro et al. (1994) has been implemented recently. The configuration of HLLC scheme is demonstrated in Fig. 1. The wave speeds are given by

$$S_L = \min(u_L - \sqrt{gD_L}, u_* - \sqrt{gD_*})$$
$$S_* = u_* \quad (21)$$
$$S_R = \max(u_R + \sqrt{gD_R}, u_* + \sqrt{gD_*})$$

where u_* and $\sqrt{gD_*}$ are estimated by

$$u_* = \frac{1}{2}(u_L + u_R) + \sqrt{gD_L} - \sqrt{gD_R}$$
$$\sqrt{gD_*} = \frac{\sqrt{gD_L} + \sqrt{gD_R}}{2} + \frac{u_L - u_R}{4} \quad (22)$$

The HLLC flux can be written as

$$\mathbf{F}^{hllc} = \begin{cases} \mathbf{F}_L & \text{if } S_L \geqslant 0 \\ \mathbf{F}_L + S_L(\mathbf{U}_L^* - \mathbf{U}_L) & \text{if } S_L < 0 < S_* \\ \mathbf{F}_R + S_R(\mathbf{U}_R^* - \mathbf{U}_R) & \text{if } S_* < 0 < S_R \\ \mathbf{F}_R & \text{if } S_R \leqslant 0 \end{cases} \quad (23)$$

3. Model validations

3.1. Lock-exchange problem

The model was first tested against an exchange flow using the parameters of direct numerical simulations (Härtel et al., 2000) and several nonhydrostatic studies (Fringer et al., 2006; Lai et al., 2010). The computational domain is two-dimensional with length $L = 0.8$ m and depth $D = 0.1$ m, which is discretized by 800×100 grid cells with $\Delta x = \Delta y = 0.001$ m. The horizontal and vertical molecular viscosities are $v_h = v_v = 10^{-6}$ m²/s. The eddy viscosities are zero. The sediment settling velocity is assumed to be zero. All the boundaries except the free surface are free-slip. In the simulation, the density of the fluid is correlated with sediment concentration, which is adjusted to generate the initial density of the light fluid as $\rho_1 = 999.972$ kg/m³ and that of the heavy fluid as $\rho_2 = 1000.991$ kg/m³, following Lai et al. (2010). Thus, the density difference of the light and heavy fluids gives a reduced gravity of

$$g' = g\Delta\rho_m/\rho_0 = 0.01 \text{ m/s}^2 \quad (24)$$

Both HLLC and HLL schemes are employed in the simulation. Fig. 2 shows the comparison of the resulting density distributions using different numerical schemes after 15.0 s. As we can see, the lock exchange flow and the generation of Kelvin–Helmholtz billows are better captured by HLLC scheme. Less billows are developed with
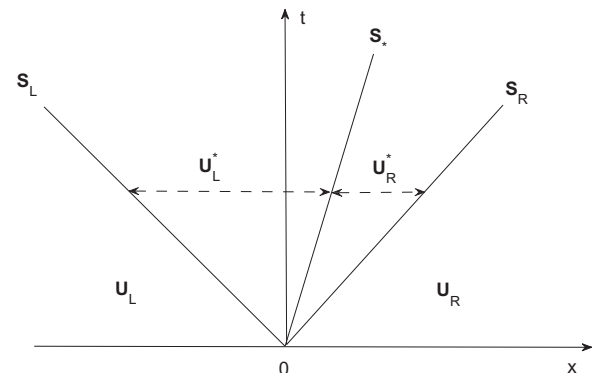

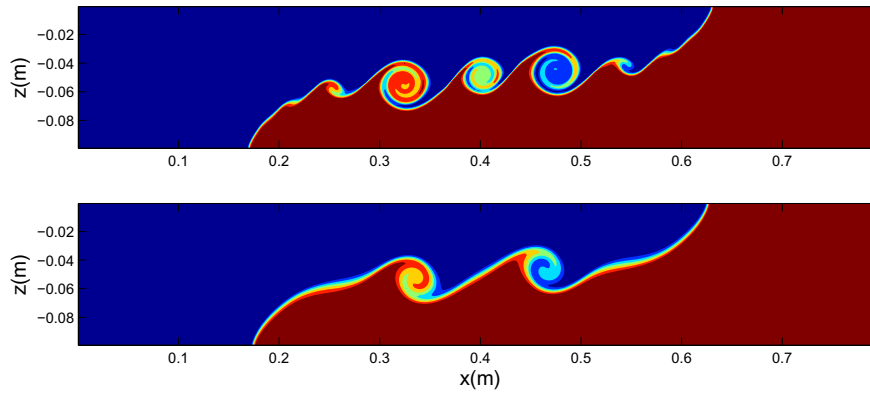**Fig. 1.** Configuration for the HLLC approximate Riemann solver.

Fig. 2. Comparison of the resulting density distributions using HLLC (upper panel) and HLL scheme (lower panel) for lock exchange problem after 15.0 s.

HLL scheme because of the high numerical diffusion. Fig. 3 presents the time series of overflow and underflow velocities using different schemes. With HLLC scheme, the maximum overflow and underflow velocities before hitting the wall are 1.83 cm/s and 1.70 cm/s, which are very close to the theoretical value of 1.59 cm/s (Fig. 3). The HLL scheme is less accurate than HLLC scheme. Although its numerical diffusion is high, HLL scheme can also predict the overflow and underflow in reasonable accuracy.

3.2. Turbidity currents

In this section, the model's capability for simulating turbidity currents is evaluated. Specifically, the model is employed to simulate the laboratory experiments reported by García (1993), who conducted measurements on both sediment and saline driven currents. The present paper is only focused on the sediment driven cases. The laboratory experiments were conducted in a 30 cm wide, 78 cm deep and about 12 m long flume. The experiment configuration involved a bed slope transition. Dense turbid water was introduced through an inlet onto an inclined bed with a slope of

0.08, which was connected with a 6.6 m long horizontal bed. In many cases, the turbidity currents experienced a hydraulic jump at the slope transition. A set of experimental runs were carried out by varying sediment size, sediment concentration and inlet velocity. For model validation, two series of experiments (NOVA7 and DAPER) are presented. These cases have also been applied to validate a two-phase sediment transport model by Snyder and Hsu (2011).

Similar to Snyder and Hsu (2011), two series of 2DV simulations are conducted. The domain is chosen to be 10 m long. The water depth of upstream boundary is 0.4 m, and that of downstream part is 0.8 m. The grid size in the streamwise direction is 0.02 m. 100 vertical layers are employed in the simulations. The inlet is located at the left boundary with height of 3 cm, which is roughly resolved by 8 vertical layers. For case NOVA7, the turbidity current at the inlet has a velocity of $U_0 = 11$ cm/s with the volumetric concentration $\phi_0 = 0.0073$. Fig. 4 shows the snapshots of simulated turbidity currents at $t = 100$ s and $t = 150$ s, which are visualized through the distributions of sediment concentrations. The mass concentration C is correlated with the volumetric concentration
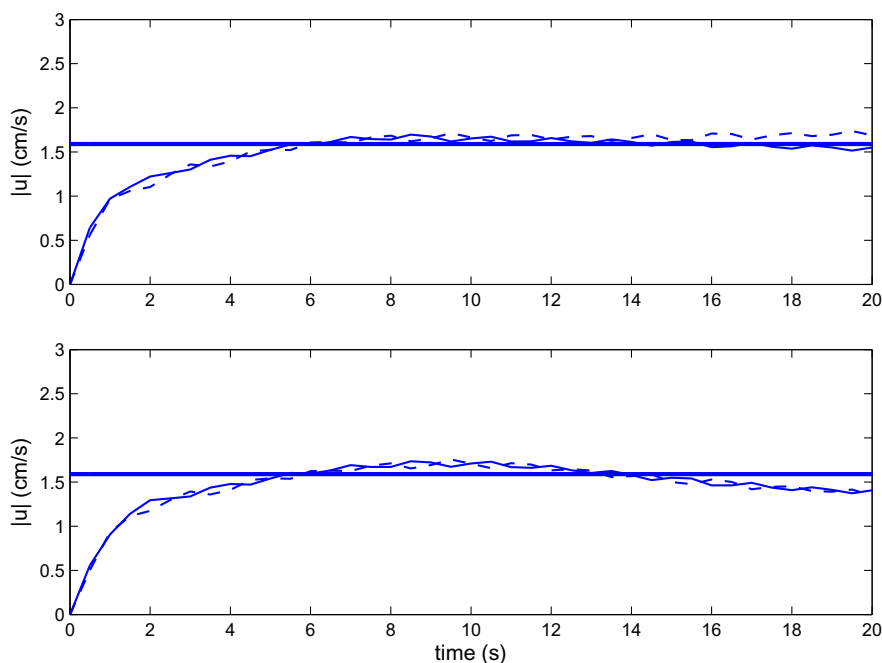

Fig. 3. Time series of surface (dashed line) and bottom (solid line) horizontal velocities measured at the midpoint of the computational domain with HLLC (upper panel) and HLL scheme (lower panel). Heavy solid line indicates the velocity derived from the energy balance theory (Turner, 1973).
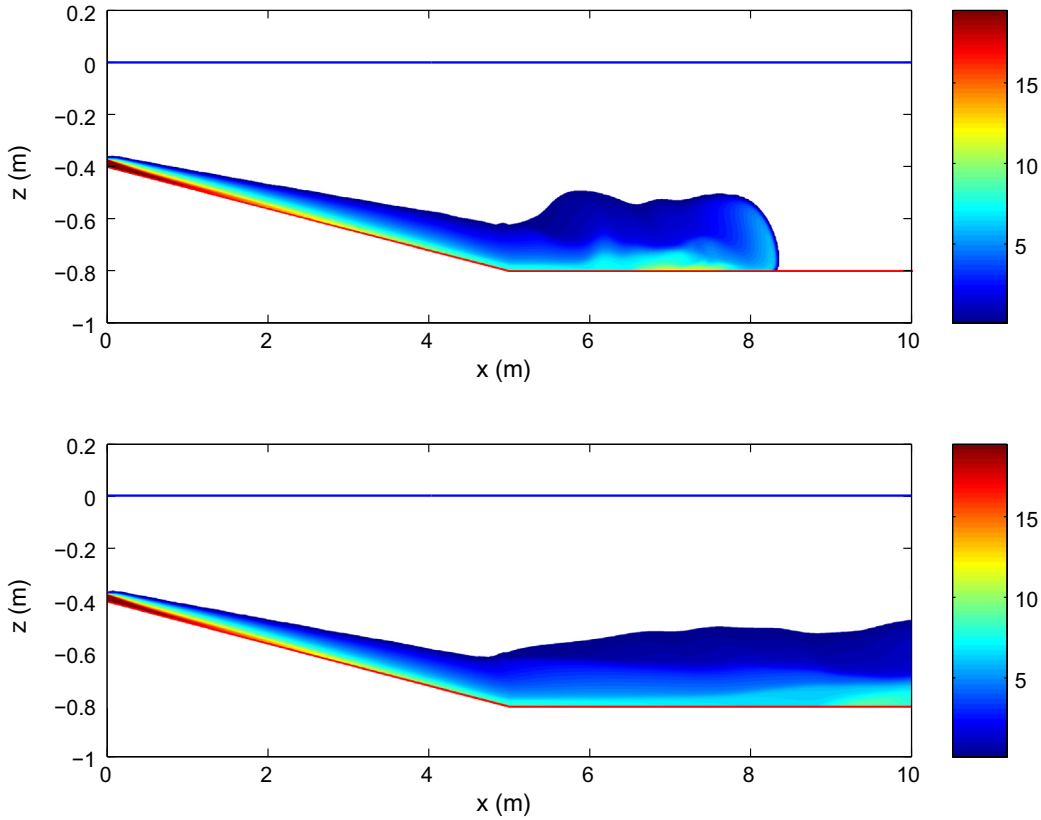
Fig. 4. Sediment concentration distributions for case NOVA7 of García (1993) at t = 100 s and 150 s. The inlet is located at the left boundary with height of 3 cm. The inlet flow velocity is 11 cm/s, and sediment concentration is 19.345 kg/m^3.

via $C = \rho_s \phi$. The flow structures observed in the experiment are well reproduced by the present model. The internal hydraulic jump, where the turbidity current changes from upstream supercritical to downstream subcritical condition, is clearly seen at the slope transition.

Model-data comparisons of velocity profiles at both supercritical ($x = 3$ m) and subcritical ($x = 8$ m) regions for case NOVA7 are presented in Fig. 5. The velocities and vertical coordinate are respectively normalized by the layer-averaged velocity $<u>$ and layer thickness h_s, which are defined as

$$<u> = \frac{\int_{-h}^{\eta} u^2 dz}{\int_{-h}^{\eta} u dz} \tag{25}$$

and

$$h_s = \frac{\left(\int_{-h}^{\eta} u dz\right)^2}{\int_{-h}^{\eta} u^2 dz} \tag{26}$$

It is clearly shown that the simulations agree well with the measurements at both locations, indicating that the model is capable of capturing the internal hydraulic jump at the slope transition. In the upstream supercritical region, the boundary layer extending to the maximum velocity point covers a small portion of the current thickness, while 80% of the flow is unbounded. The thickness of boundary layer is greatly increased in the case of subcritical flow, which covers about 50% of the current layer.

We also carried out model-data comparisons of DAPER series (DAPER1, DAPER2 and DAPER6). All the DAPER series have the inlet velocity of $U_0 = 8.3$ cm/s. The inlet sediment concentrations of
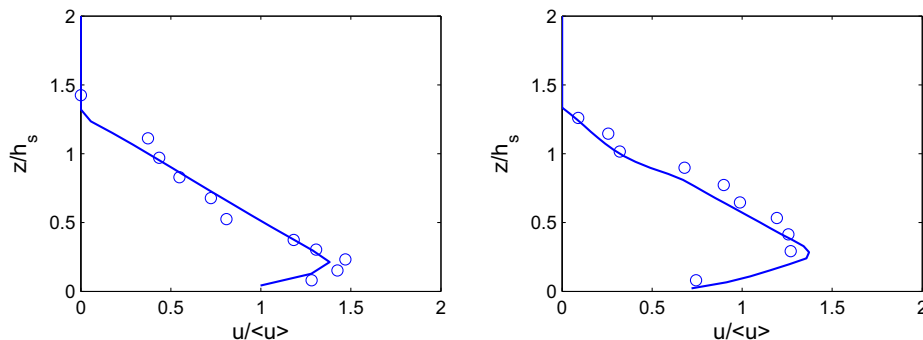

Fig. 5. Comparisons of simulated (solid lines) and measured (circles) current velocities of case NOVA7 at supercritical (left panel) and subcritical (right panel) regions, which are located at 300 and 800 mm downstream from the inlet. The measurement data were reported by García (1993). The velocities are normalized by the layer-averaged velocity $<u>$.The vertical coordinate is normalized by the layer thickness h_s.

these three runs are $\phi_0 = 0.00143$, 0.00183 and 0.00372, respectively. Again, the results are normalized by the layer-averaged values. The layer-averaged sediment concentration $< C >$ is calculated by

$$< C >= \frac{\int_{-h}^{\eta} uCdz}{\int_{-h}^{\eta} udz} \tag{27}$$

Fig. 6 shows the comparisons of gravity current velocities and vertical sediment concentration distributions at both supercritical and subcritical regions. Results demonstrate that the model predicts the flow velocities as well as sediment concentration profiles fairly well at both locations. These comparisons prove that the model is capable of simulating flow-sediment interactions, and can be applied to study gravity current induced flow problems.

4. Tsunami waves generated by landslides

4.1. Waves generated by a small-scale landslide

In this section, we present a numerical simulation of water waves generated by a laboratory landslide. The experiments were described in Assier-Rzadkiewicz et al. (1997). A series of experiments were conducted by allowing a mass of sand to slide freely down an inclined plane with varying slope and sediment diameter. We have chosen to simulate the case of a volume of 63,000 cm³ of coarse gravel sliding down a 45° slope. The model setup is the same as that of Assier-Rzadkiewicz et al. (1997), shown in Fig. 7. The computational domain is 4 m (-1 m $\leqslant x \leqslant 3$ m) long, which is discretized by 400 grids with $\Delta x = 0.01$ m. The water depth is 1.60 m and the top of the slide is initially 10 cm below the water surface. The dimensions of the slide is 0.65 m × 0.65 m. The mean apparent density is 1950 kg/m³, resulting in the volumetric sedi-

ment concentration of 0.58. 25 vertical layers are used in the simulation.

Fig. 8 shows the comparisons of simulated and measured surface elevations at $t = 0.4$ s and $t = 0.8$ s. In the simulation, the water–sediment mixture is modeled as turbulent fluid without rheology. The turbulent viscosity and diffusivity are calculated by the $k-\epsilon$ model. We can see that the model over-predicts the surface waves generated by the underwater landslide. The discrepancies are introduced by the simplified treatment of the landslide, in which intergranular stresses which could retard the initial failure of the sliding mass are neglected. In the experiment, the majority of the sand remains close to the initial position at $t = 0.4$ s. In the simulation, however, mass failure of the entire slide occurs in the first instant. As demonstrated in Fig. 9, the simulated slide mass is mainly concentrated at the slide front, which is not the case in the experiment (Assier-Rzadkiewicz et al., 1997). More accurate simulation of the laboratory underwater landslide would require a more thorough consideration of the rheological behavior of the granular material, which is left for future studies. In Fig. 8, we also present the numerical results of Assier-Rzadkiewicz et al. (1997) using NASA-VOF2D, which considers the mudslide as a Bingham material. At the early stage of the landslide ($t \leqslant 0.4$ s), the surface waves generated by these two models are similar. After 0.4 s the slide movement predicted by the present model is slightly faster, which results in larger surface waves. Generally, these two models predict comparable results. However, the present model utilizes a much coarser vertical grid resolution and is thus expected to be more computationally efficient.

4.2. Waves generated by a large-scale landslide

In this section, we replicate an example landslide described in Jiang and Leblond (1992) and investigate the effects of different
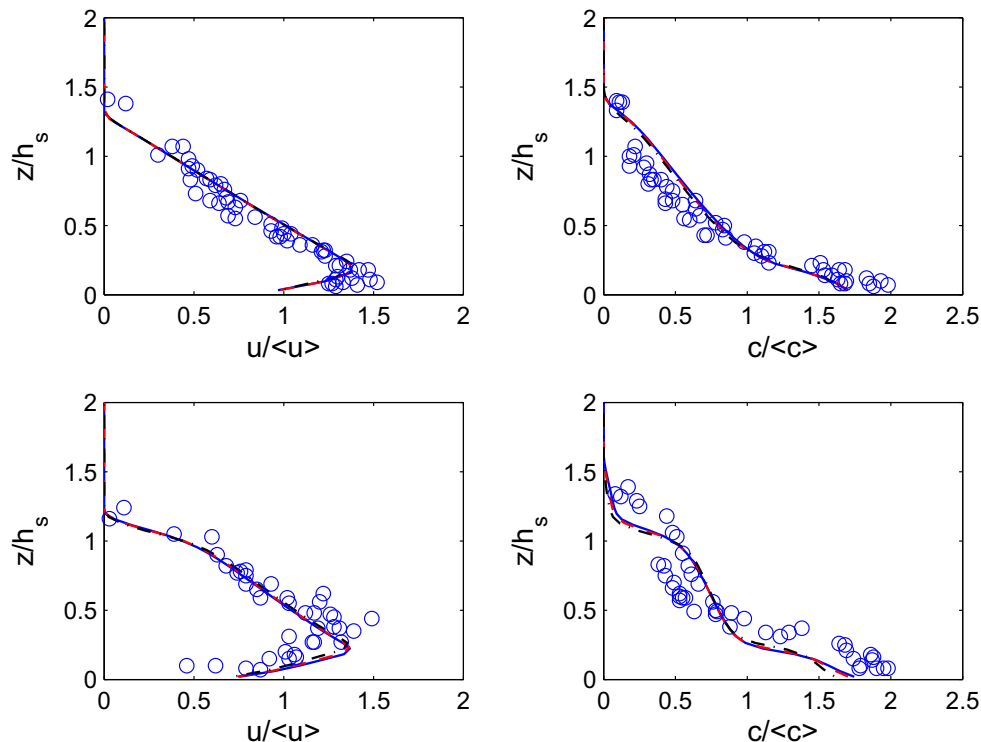

Fig. 6. Comparisons of simulated and measured current velocities (left panels) and sediment concentrations (right panels) of case DAPER at supercritical and subcritical regions, which are located at 300 and 800 mm downstream from the inlet. The measurement data were reported by García (1993). The velocities and sediment concentrations are normalized by layer-averaged velocity $< u >$ and concentration $< c >$, respectively. The vertical coordinate is normalized by the layer thickness h_s. Circles: data; Solid lines: DAPER1; Dashed lines: DAPER2; Dash-dotted lines: DAPER6.
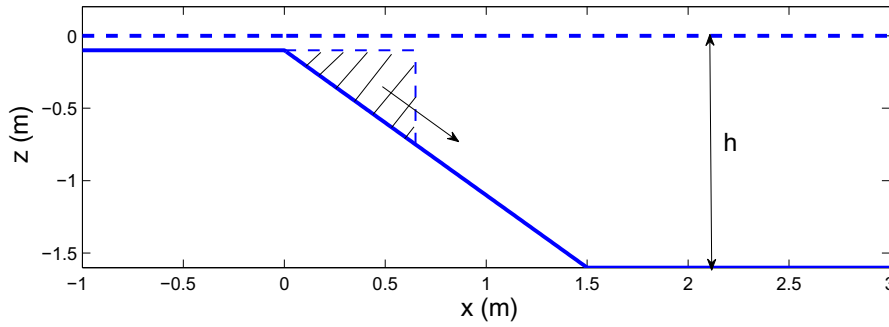
Fig. 7. The computational domain and model setup for water wave generation by a laboratory landslide. The water depth is $h = 1.60$ m. The slope of the inclined plane is 45°. The shadow region shows the initial location of landslide. The mean apparent density of the landslide is 1950 kg/m³.
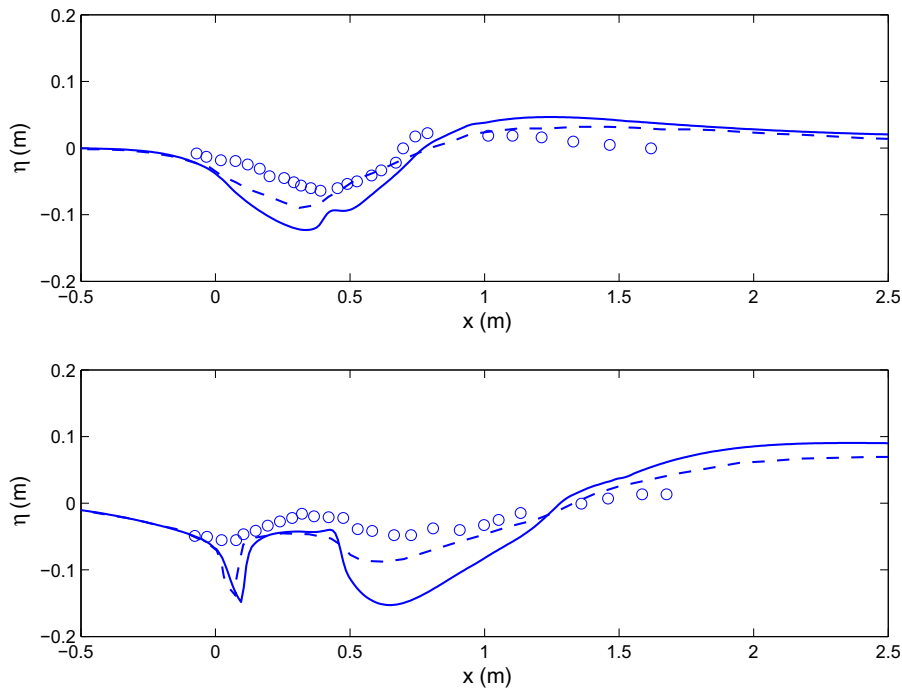

Fig. 8. Comparisons of simulated and measured surface elevation at $t = 0.4$ s (upper panel) and $t = 0.8$ s (lower panel). Circles: measurements; Solid lines: current model; Dashed lines: Assier-Rzadiewicz Assier-Rzadkiewicz et al. (1997).

parameters on the surface tsunami waves as well as slide motion. We shall focus on the two-dimensional problem first. Fig. 10 presents the computational domain and model setup. The computational domain has a minimum water depth of 12 m and a maximum water depth of 400 m. The landslide is located at a gentle uniform slope with inclination $\theta = 4°$. The slide is initially at rest and has a parabolic surface given by

$$H = T(1 - [2(x - \bar{x})/L]^2) \tag{28}$$

where $T = 24$ m is the initial maximum landslide height, $L = 686$ m is the initial length of the slide, H is the slide height at coordinate $x, \bar{x}$ is the initial coordinate of the centroid.

In the numerical simulations, the landslide is modeled as a water–sediment mixture without rheology. The domain is discretized by 2000 horizontal grids and 40 vertical layers in order to better capture the slide movement. Eleven model runs are conducted by varying slide density ρ_{slide}, settling velocity of sediment w_s and initial location of the slide h_{slide}. The details of the model parameters are shown in Table 1. The simulation time is 120 s. All the simulations were carried out in the the high performance computing

(HPC) community cluster mills.hpc.udel.edu at University of Delaware using 8 processors. The typical time required for each simulation is about 17 h.

Fig. 11 illustrates the evolution of surface waves generated by the underwater landslide for run 2d. The landslide is initially located at 120 m water depth. The slide density is 2000 kg/m³. The settling velocity of the sediment is chosen as 0.1 m/s. At the beginning of the landslide, a single wave with nearly symmetric crest and trough is generated. As the mud slides further downward along the slope, three wave trains are produced. The first wave train is led by a large wave crest, which propagates into the deeper water with speed faster than the slide motion. The second wave train follows the first one as a forced wave train propagating with the speed of the slide. This wave train consists of relatively shorter dispersive waves. The wave height of the leading wave can be larger than the wave crest in the first wave train. The third wave train is a small trough propagating shoreward. The three wave trains generated by the underwater landslide were also found by Jiang and Leblond (1992). However, shallow-water equations were solved in their studies, which were not able to capture the dispersive waves.
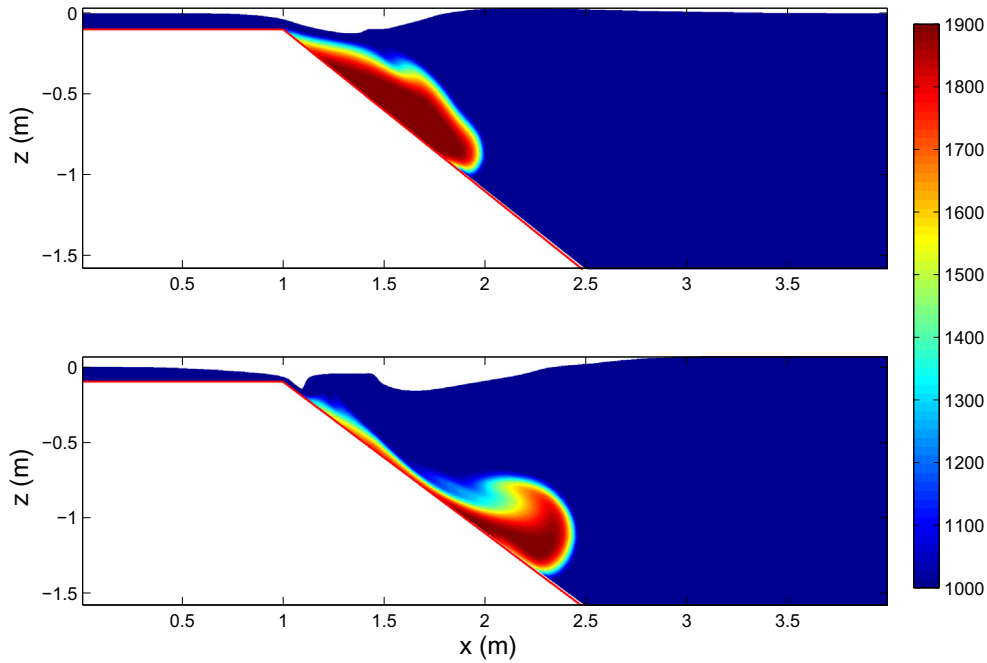
Fig. 9. Snapshots of simulated density distributions at $t = 0.4$ s (upper panel) and $t = 0.8$ s (lower panel).
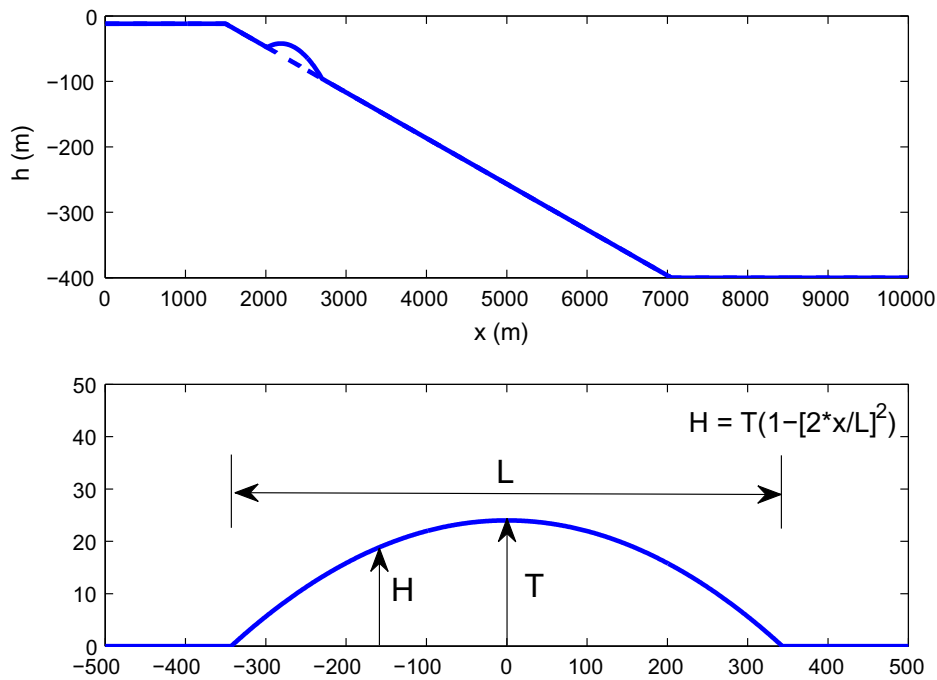

Fig. 10. Sketch of the initial landslide, which is described by $H = T(1 - [2(x - \bar{x})/L]^2)$, where T is the initial maximum landslide height, L is the initial length of the slide, H is the slide height at coordinate x. The computational domain has a minimum water depth of 12 m and a maximum water depth of 400 m. The landslide is located at a gentle uniform slope with inclination θ.

In Fig. 11, we also present the mesh dependence of the simulated tsunami waves. Two meshes are tested. One is using 2000 horizontal grids and 40 vertical layers with $dx = 5$ m. The other is using 1000 horizontal grids and 40 vertical layers with $dx = 10$ m. We can clearly see the convergence of the numerical results with mesh refinement, although there is minor difference in the wave train that is tied to the landslide motion (second wave train). This wave train consists of relatively short waves, which are more sensitive to the grid resolution.

A wave energy analysis is conducted as well to investigate how the deformable landslide transfers energy to the surface waves. To see how wave energy is distributed over the three wave trains, we particularly take a look at the wave energy at $t = 100$ s, when the three wave trains can be easily separated. For a crude estimation, we divided the domain into three regions. Region 1 is from $x = 0$ to 3000 m, containing the onshore moving wave train. Region 2 is from 3000 m to 5000 m, where the wave train tied to the landslide is located. Region 3 includes the area with $x > 5000$ m, where

Table 1
Parameters for different model runs, Section 4.2.

Case	ρ_{slide} (kg/m^3)	w_s (m/s)	h_{slide} (m)
1a	1200	0.1	120
1b	1400	0.1	120
1c	1600	0.1	120
1d	1800	0.1	120
2a	2000	0.1	60
2b	2000	0.1	80
2c	2000	0.1	100
2d	2000	0.1	120
3a	2000	0.01	120
3b	2000	0.001	120
3c	2000	0.0	120

the offshore moving wave train is located. The energy (potential energy and kinetic energy) contained in these three regions are 2.79×10^8 J, 3.88×10^{10} J, 2.72×10^9 J, respectively. These results indicate that the landslide transfers most of its energy to the wave train concomitant with the landslide motion, which accounts for about 93% of the total energy.

Fig. 12 demonstrates the evolution of the underwater landslide for run 2d. Sediment suspension is not significant during the slide motion. At the beginning of the landslide, the slide moves as a thin fluid sheet with most of sediment constrained close to the bottom. As the mud slides downward, more and more sediment is accumulated in the front, producing a bulbous front where a strong vortex is developed. The slide front is always concomitant with the large wave trough in the second wave train.

4.2.1. Effect of sediment settling velocity

The sediment settling velocity or sediment size is always considered as one of the most important parameters affecting sediment transport and associated physical processes. It directly determines sediment suspension and deposition in a sediment-

laden turbulent flow. Its effects on landslide motion and the surface waves which it generates are examined in this section.

Fig. 13 shows the surface waves generated by the underwater landslide with different sediment settling velocity w_s. Four settling velocities are examined in this study. It is noticed that the effects of sediment settling velocity on the first and third wave trains are minor. Considering that the sediment settling velocity primarily affects the slide deformation, this result is consistent with earlier studies by Grilli and Watts (2005), who found that the slide initial acceleration governs the generation of the offshore and onshore moving wave trains, while the slide deformation does not have significant effects on these two wave trains. The effect of sediment settling velocity on the second wave train is significant. This wave train is possibly governed by the slide deformation. Larger settling velocity would result in larger leading waves and faster wave speed, indicating that the mud slides faster with larger settling velocity (or sediment size) as shown in Fig. 14. For settling velocity $w_s = 0.1$ m/s, more sediment is concentrated on the slide front (Fig. 14a), which produces significant baroclinic pressure gradient. Consequently, the turbidity current driving mud transport is stronger. From Fig. 13, we also notice that the surface waves are not sensitive to the sediment setting velocity when its value becomes less than 0.01 m/s.

Fig. 15 presents the effects of w_s on the evolution of frontal speed of the mud V_{slide} (the maximum landslide velocity), local Froude number $Fr = V_{slide}/\sqrt{gh_{local}}$ as well as the maximum wave amplitude $|\eta|_{max}$. The local water depth h_{local} is defined as the water depth at which the maximum landslide velocity is found. Clearly, two stages of slide motion can be discerned. The first stage is the acceleration stage, during which the frontal speed of the slide becomes increasingly larger. The frontal speed approaches its maximum value approximately at $t = 50$ s. During this stage, the effects of settling velocity w_s on $|\eta|_{max}$ are negligible. $|\eta|_{max}$ is found at the offshore moving wave train (first wave train). However, it does affect the slide motion. Larger settling velocity would result in slightly faster landslide motion. The second stage corresponds
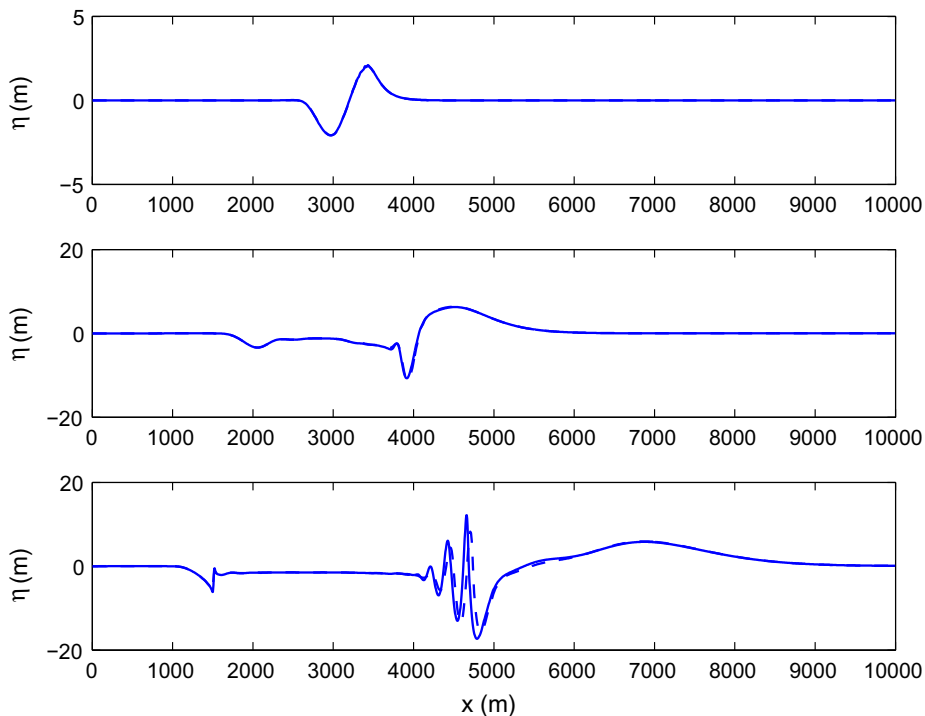

Fig. 11. Tsunami waves generated by the landslide at (a) $t = 10$ s; (b) $t = 50$ s and (c) $t = 100$ s for run 2d with two meshes. The initial water depth of the slide is 120 m. The density of the landslide is 2000 kg/m^3. The settling velocity of sediment is 0.1 m/s. Solid line: mesh 1 (2000×50); dashed line: mesh 2 (1000×50).
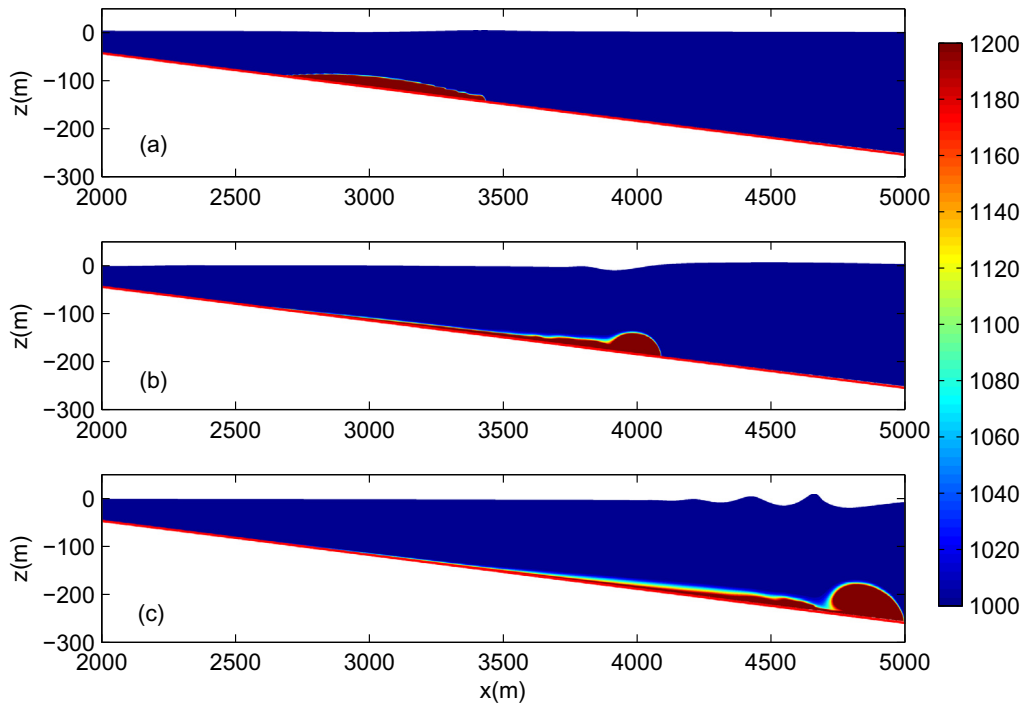
Fig. 12. The motion of the landslide illustrated as the distributions of sediment concentration at (a) $t = 10$ s; (b) $t = 50$ s and (c) $t = 100$ s for run 2d. The initial water depth of the slide is 120 m. The density of the landslide is 2000 kg/m^3. The settling velocity of sediment is 0.1 m/s.
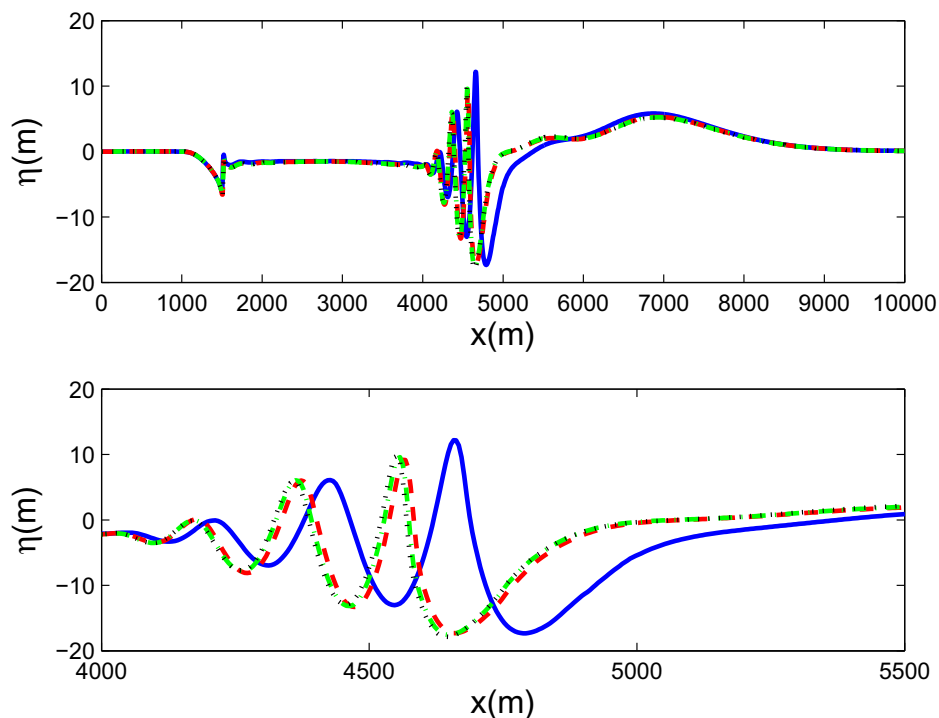

Fig. 13. Effects of the sediment settling velocity w_s on tsunami wave generation at $t = 100$ s. The lower panel is a blow-up view of the waves tied to the landslide. The initial water depth of the slide is 120 m. The density of the landslide is 2000 kg/m^3. Solid line: $w_s = 0.1$ m/s; dashed line: $w_s = 0.01$ m/s; dash-dotted line: $w_s = 0.001$ m/s; dotted line: $w_s = 0.0$ m/s.

to constant frontal speed. During this stage, the effects of sediment settling velocity on $|\eta|_{max}$ are noticeable if its value is greater than 0.01 m/s. The evolution of the Froude number is similar to that of the frontal speed. The mudflow is subcritical with Froude number less than 1.0. There is a clear decay of the wave height after reaching its peak value. Again, the temporal variation of maximum wave amplitude is not significantly affected by the sediment settling velocity with values less than 0.01 m/s.
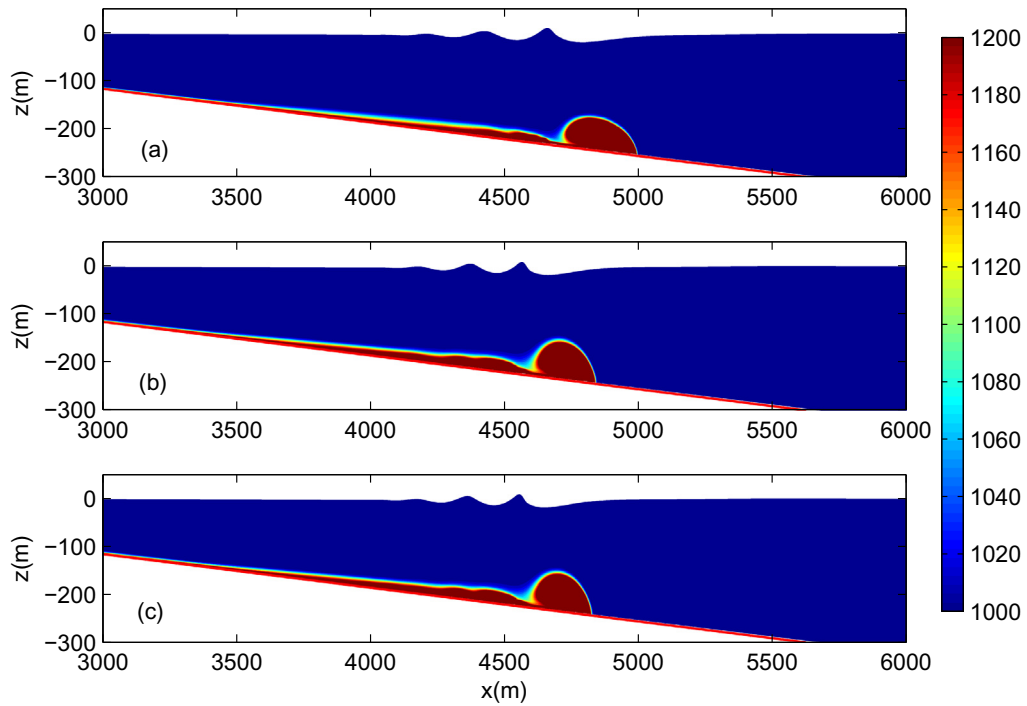
Fig. 14. Effects of the sediment settling velocity w_s on landslide motion at $t = 100$ s. The initial water depth of the slide is 120 m. Other conditions are referred to Table 1. (a) $w_s = 0.1$ m/s; (b) $w_s = 0.01$ m/s and (c) $w_s = 0.001$ m/s.
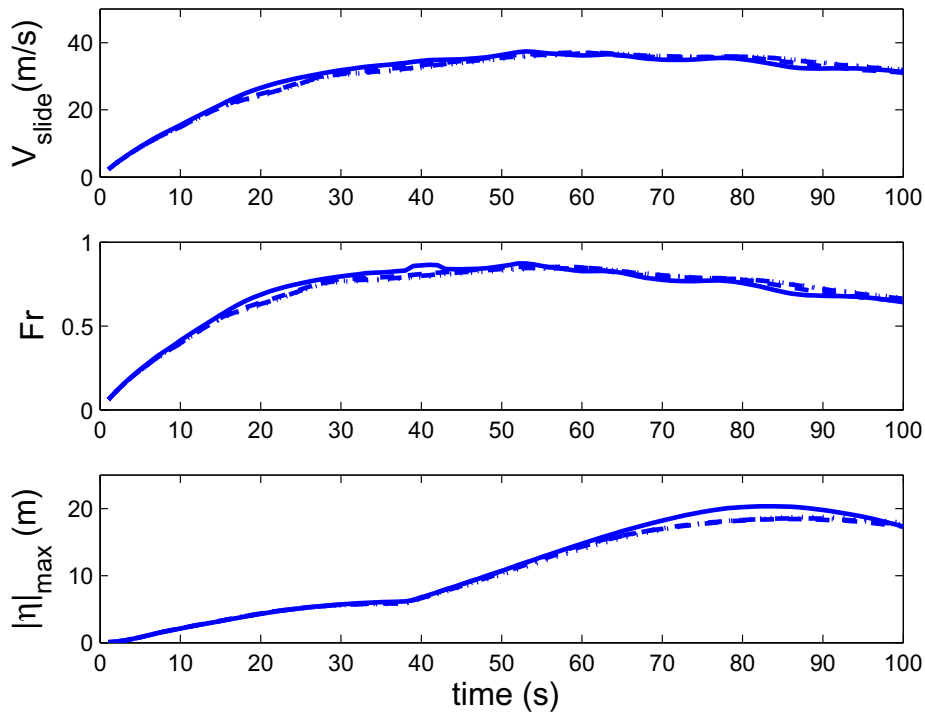

Fig. 15. Effects of the sediment settling velocity w_s on the frontal speed of the landslide V_{slide}, local Froude number $Fr = V_{slide}/\sqrt{gh_{local}}$ as well as surface wave amplitude $|\eta|_{max}$. Solid line: $w_s = 0.1$ m/s; Dashed line $w_s = 0.01$ m/s; Dash-dotted line: $w_s = 0.001$ m/s and Dotted line: $w_s = 0.0$ m/s.

4.2.2. Effect of initial depth of the landslide

The effect of initial water depth of the landslide on the surface tsunami waves was previously investigated by Jiang and Leblond (1992). They found that, for larger initial depth of the landslide, the interactions between the landslide and surrounding water are weaker, and surface waves generated by the landslide are smal-

ler. This is further confirmed in the current study, in which simulations with four initial depths of the landslide are conducted. Fig. 16 shows the surface waves generated by the landslides initially located at $d = 60$, 80, 100 and 120 m at $t = 100$ s. In order to better compare waveforms, we plot the figures with $x - x_{ini}$ as x-axis, where x_{ini} is the initial location of the landside. Clearly,
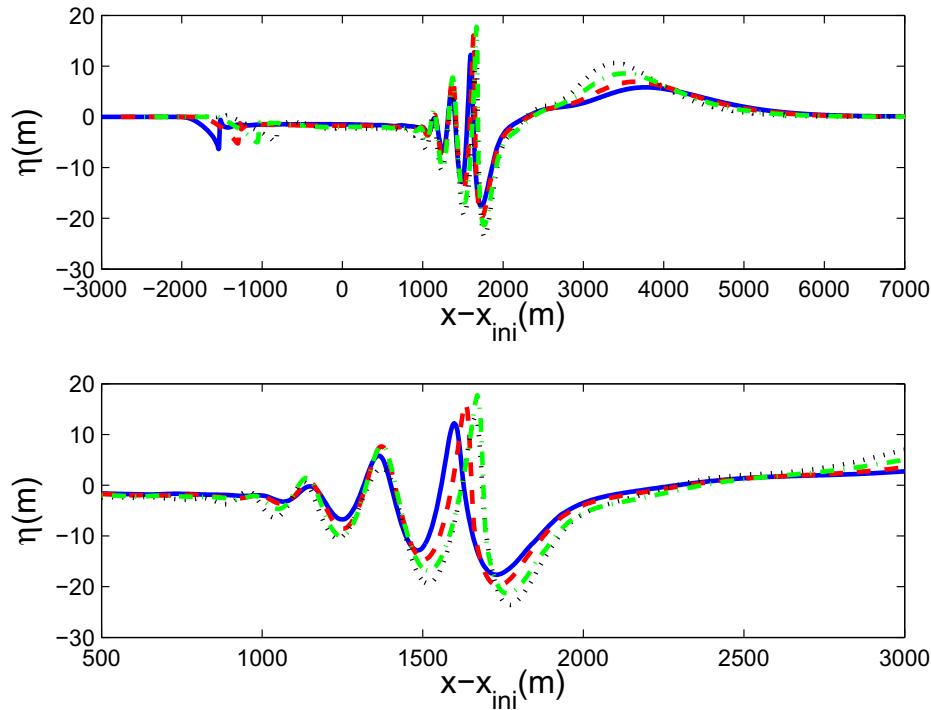
Fig. 16. Effects of initial water depth of the slide on tsunami wave generation at $t = 100$ s. The lower panel is a blow-up view of the waves tied to the landslide. x_{ini} is the initial location of the landslide. Other conditions are referred to Table 1. Solid line: $d = 120$ m; dashed line: $d = 100$ m; dash-dotted line: $d = 80$ m; dotted line: $d = 60$ m.

the landslide located at the shallower water depth can generate larger surface waves, which can be observed in all three wave trains. This indicates that the slide–water interactions are more significant for shallower landslides. It is interesting to see that the offshore and onshore wave trains generated by deeper landslide propagate faster, while the wave train tied to the landslide travels faster with a shallower landslide. It seems that deeper landslide can generate longer onshore and offshore moving waves.

The effects of initial water depth on the frontal speed, the Froude number as well as the maximum surface wave amplitude are presented in Fig. 17. It can be seen that the landslide frontal speed is seldom affected by the initial water depth. Thus, the Froude number is larger for shallower landslide, which tends to produce larger surface waves. Similar to the findings of Abadie et al. (2012), the wave generation process is more efficient if the Froude number Fr is larger. The distributions of mixture density and land-slide motion are presented in Fig. 18 for $d = 60$ m, 100 m, 120 m, from which we can also see more significant interaction between surface waves and shallower landslide.

4.2.3. Effect of slide density

The density of the landslide is one of the dominant parameters controlling slide movement as well as surface waves which it generates. Higher density of the landslide produces larger baroclinic pressure gradient, subsequently generating faster frontal speed and larger surface waves. This is demonstrated in Fig. 19, which compares the surface waves generated by four landslides with $\rho_{slide} = 1400$ kg/m³, 1600 kg/m³, 1800 kg/m³, 2000 kg/m³, respectively. All the landslides are initially located at 120 m water depth with sediment settling velocity $w_s = 0.1$ m/s. We can see that the surface waves including all three wave trains are significantly affected by the mud density. The surface wave heights are larger with higher mud density. For the mud density $\rho_{slide} = 1400$ kg/m³, the wave trains seem to be non-dispersive. The effects of mud density on landslide motion are demonstrated in Fig. 20.

Clearly, with larger mud density, the sediment concentration at the slide front is higher, and the landslide moves faster. The interactions between the landslide and surrounding water are stronger as well.

Fig. 21 displays the temporal variations of the frontal speed of the landslide V_{slide}, the Froude number Fr as well as the maximum wave amplitude $|\eta|_{max}$ with different mud densities. The slide density has much more significant effects on surface waves as well as landslide motion than the settling velocity and initial slide depth. With larger mud density, the frontal speed is consistently faster. The Froude number of the landslide and the maximum wave amplitude are also larger. As the slide density is increased from 1400 kg/m³ to 2000 kg/m³, the frontal speed of the landslide can be twice faster. The maximum wave amplitude can be more than four times larger.

4.3. 3D simulation of underwater landslide

A three dimensional simulation is also conducted to show the model's capability of modeling 3D landslide. The model setup is similar to that of the 2D simulation, except that the initial landslide is defined using truncated hyperbolic secant function (Enet and Grilli, 2007).

$$\zeta = \frac{T}{1 - \epsilon}[\operatorname{sech}(k_b x)\operatorname{sech}(k_w y) - \epsilon] \tag{29}$$

where $k_b = 2C/b$, $k_w = 2C/w$ and $C = a\cosh(1/\epsilon)$. The landslide has length $b = 686$ m, width $w = 343$ m and thickness $T = 24$ m. The truncation parameter is $\epsilon = 0.717$. The landslide is initially located at 60 m water depth. The slide density is 2000 kg/m³.

Fig. 22 shows the temporal variation of surface waves generated by the 3D deformable landslide. We can see that the water waves are very dispersive. The directional spreading of the waves is significant, which is partly due to the spreading of the mud across the inclined plane. The wave height is much smaller than that from the 2D simulation. The surface elevations at a vertical transect with
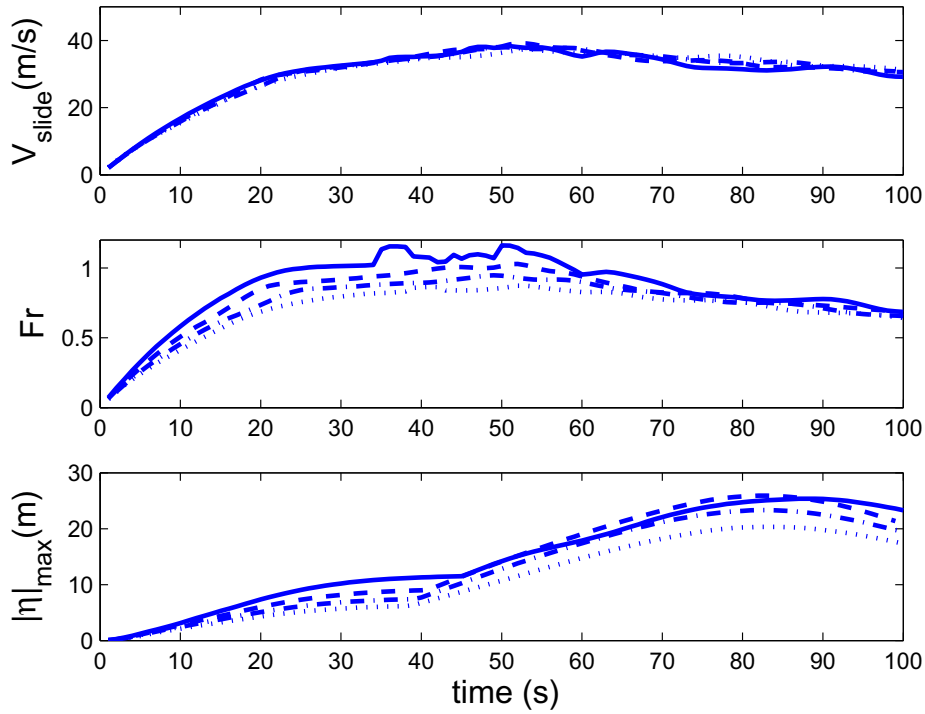
Fig. 17. Effects of initial slide depth on the frontal speed of the landslide V_{slide}, local Froude number $Fr = V_{slide}/\sqrt{gh_{local}}$ as well as surface wave amplitude $|\eta|_{max}$. Solid line: $d = 60$ m; Dashed line: $d = 80$ m; Dash-dotted line: $d = 100$ m; Dotted line: $d = 120$ m.
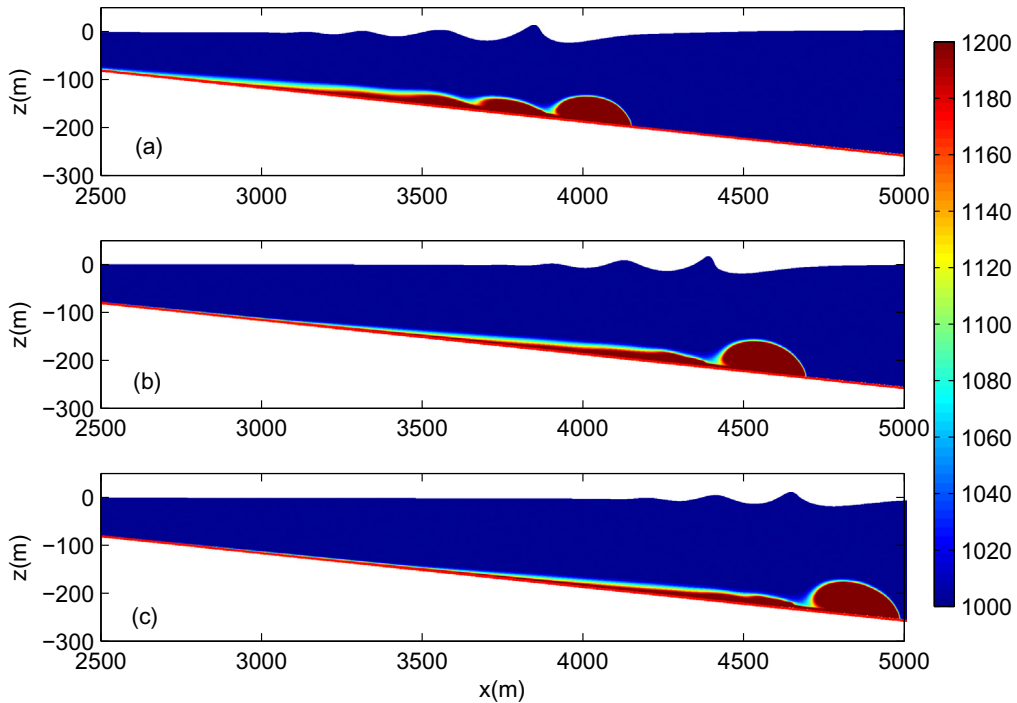

Fig. 18. Effects of initial water depth of the slide on landslide motion at $t = 100$ s. Other conditions are referred to Table 1. (a) $d = 60$ m; (b) $d = 100$ m and (c) $d = 120$ m.

$y = 0$ m are shown in Fig. 23. The pattern of surface waves is similar to that generated by 2D landslide. Three wave trains are generated by the landslide. The first one starts with a large wave crest, which propagates faster than the landslide motion. The second wave train starts with a large wave trough, which is tied to the landslide motion. The third wave train is also a wave trough, which propagates shoreward. The wave height approaches its peak value

rapidly after the release of the landslide, then decays as the wave disperses and the sediment spreads. The non-hydrostatic pressure effects on the surface wave trains are also examined. Fig. 24 shows the free surface elevations similar to those of Fig. 23. It's not surprising that the pattern of three wave trains can also be produced by the hydrostatic simulation, which has been proven by Jiang and Leblond (1992) using a 1D shallow-water equation. However, the
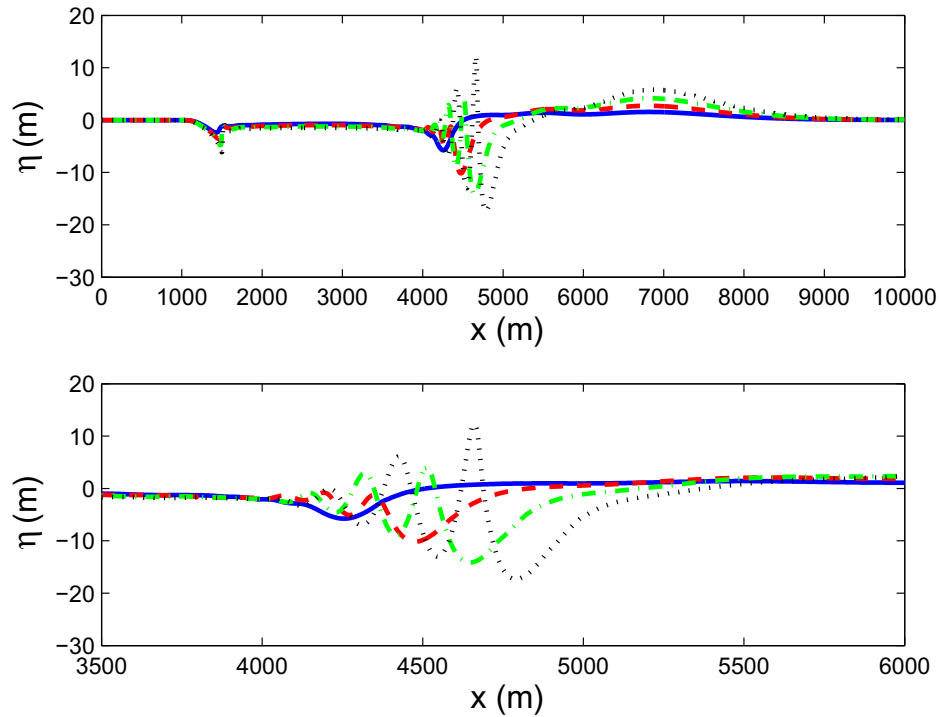
Fig. 19. Effects of slide density ρ_{slide} on tsunami wave generation at $t = 100$ s. The lower panel is a blow-up view of the waves tied to the landslide. Solid line: $\rho_{slide} = 1400$ kg/m^3; dashed line: $\rho_{slide} = 1600$ kg/m^3; dash-dotted line: $\rho_{slide} = 1800$ kg/m^3; dotted line: $\rho_{slide} = 2000$ kg/m^3.

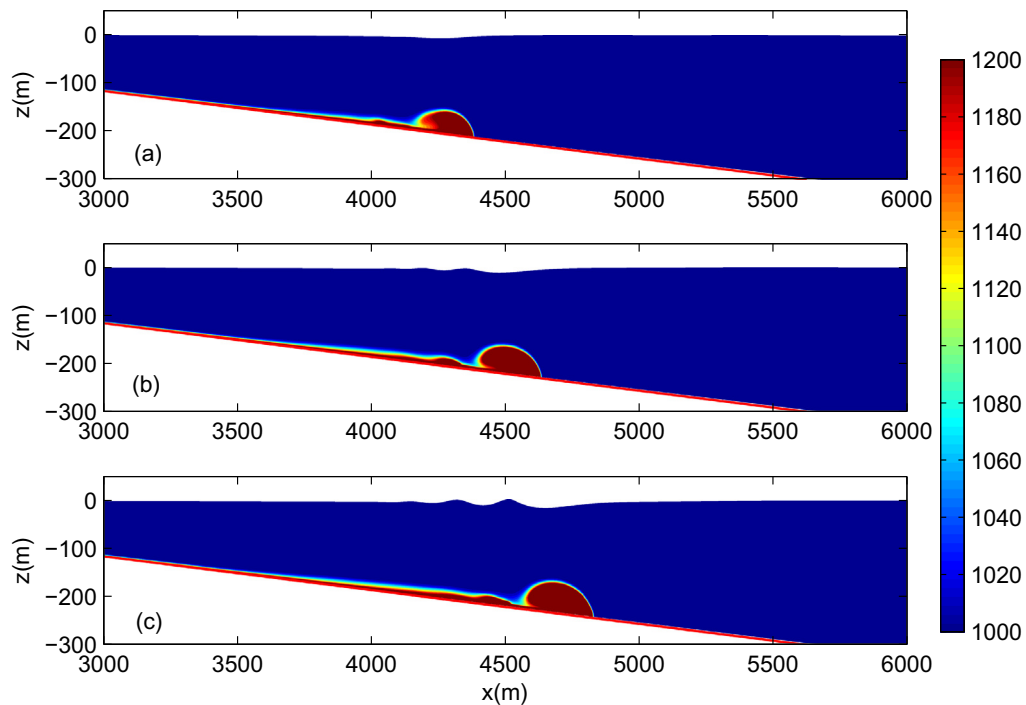**Fig. 20.** Effects of slide density ρ_{slide} on landslide motion at $t = 100$ s. (a) $\rho_{slide} = 1400$ kg/m^3; (b) $\rho_{slide} = 1600$ kg/m^3; (c) $\rho_{slide} = 1800$ kg/m^3.

wave dispersion cannot be captured by the hydrostatic simulation as clearly seen from the free surface elevation at $t = 100$ s. As a result, the wave train propagating into the deep ocean travels faster than the wave train with non-hydrostatic pressure effects.

To see the effects of deformability of the landslide on the tsunami waves, we conducted a simulation with a 3D rigid landslide.

The geometry of the rigid landslide is the same as that of the deformable one. The slide motion is prescribed based on the dynamic force balance, which is given by Enet and Grilli (2007). The displacement of the rigid landslide is described as

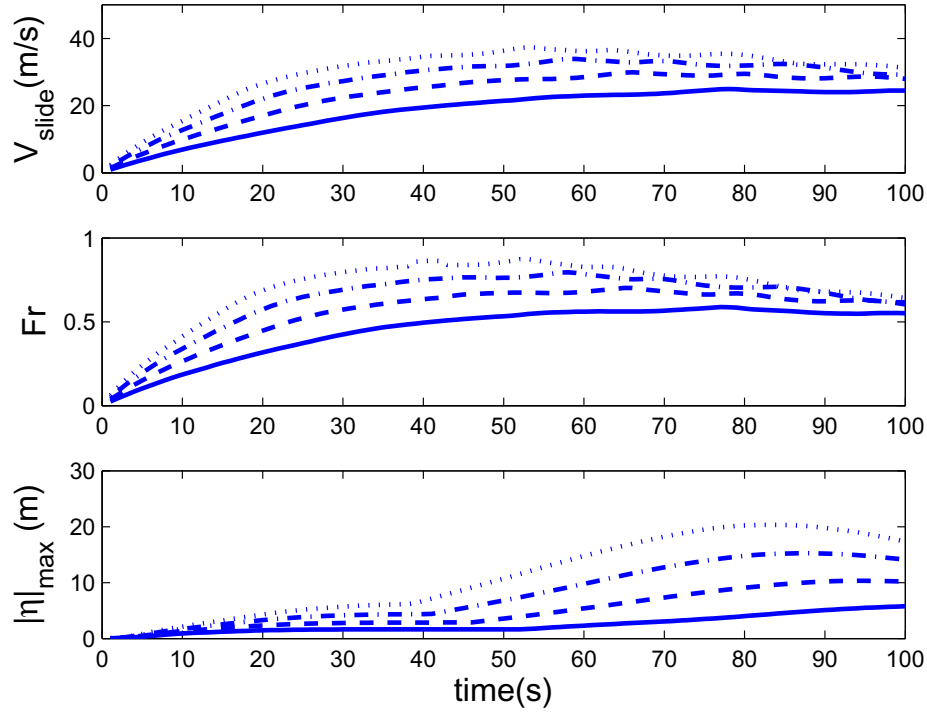$$s(t) = s_0 \ln \left(\cosh \frac{t}{t_0} \right) \tag{30}$$

Fig. 21. Effects of slide density ρ_{slide} on the frontal speed of the landslide V_{slide}, Froude number $Fr = V_{slide}/\sqrt{gh_{local}}$ and the maximum wave amplitude $|\eta|_{max}$. Solid line: $\rho_{slide} = 1400$ kg/m³; dashed line: $\rho_{slide} = 1600$ kg/m³; dash-dotted line: $\rho_{slide} = 1800$ kg/m³; dotted line: $\rho_{slide} = 2000$ kg/m³.

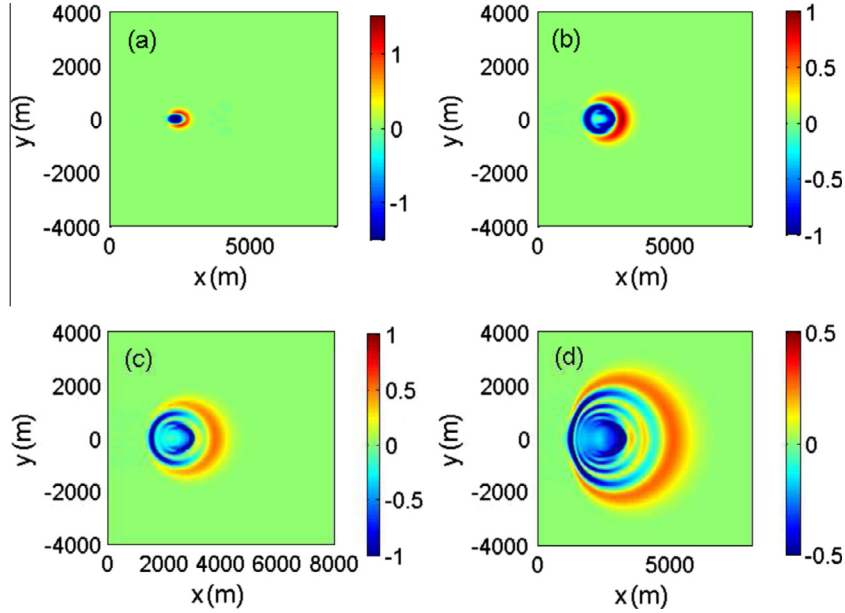**Fig. 22.** Snapshots of Tsunami waves generated by a 3D landslide at (a) $t = 10$ s; (b) $t = 30$ s; (c) $t = 50$ s and (d) $t = 80$ s. The color scales are in meters.

with the characteristic length and time of landslide motion defined as

$$s_0 = \frac{u_t^2}{a_0} \quad \text{and} \quad t_0 = \frac{u_t}{a_0} \tag{31}$$

where the initial acceleration a_0 is

$$a_0 = g \sin \theta \left(1 - \frac{\tan \phi}{\tan \theta}\right)\left(\frac{\gamma - 1}{\gamma + C_m}\right) \tag{32}$$

and the landslide terminal velocity u_t is

$$u_t = \sqrt{gd}\sqrt{\frac{b \sin \theta}{d}\left(1 - \frac{\tan \phi}{\tan \theta}\right)\frac{\gamma - 1}{C_d}\frac{2(f^2 - \epsilon)}{f - \epsilon}} \tag{33}$$

In the above equations, θ is the inclination angle of the slope which is 4° in this case. The Coulomb friction is negligible as compared to inertia, gravity and hydrodynamic forces (Enet and Grilli, 2007, such that $\phi \ll \theta$. $\gamma = \rho_s/\rho_w$ is taken as 2.0. The virtual mass coefficient C_m and drag coefficient C_d are taken as 0.5 and 1.0, respectively. With these parameters, we can obtain the initial acceleration $a_0 = 0.27$ m²/s, and the terminal velocity
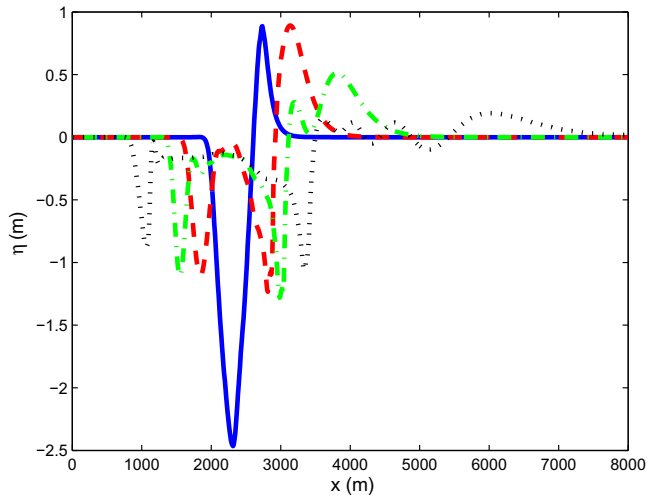
Fig. 23. Free surface elevations in a vertical plane with $y = 0$ m at $t = 10$ s (solid line); $t = 30$ s (dashed line); $t = 50$ s (dash-dotted line) and $t = 100$ s (dotted line).
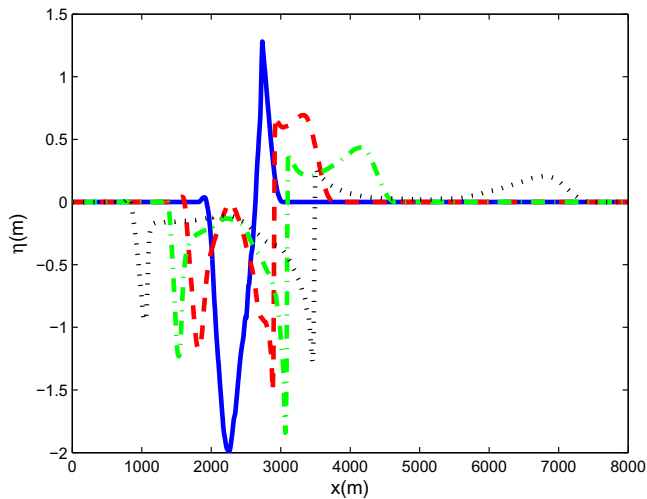

Fig. 24. Free surface elevations in a vertical plane from a hydrostatic simulation with $y = 0$ m at $t = 10$ s (solid line); $t = 30$ s (dashed line); $t = 50$ s (dash-dotted line) and $t = 100$ s (dotted line).

$u_t = 21.09$ m/s. The characteristic time of the landslide motion is $t_0 = 78.1$ s. The simulation is conducted using NHWAVE with specific boundary condition for rigid landslide, as described in Ma et al. (2012).

Fig. 25 presents the temporal variations of surface waves generated by the 3D rigid landslide. The wave forms generated by deformable (Fig. 22) and and rigid landslides are very different. For the case of rigid landslide, wave energy is mainly concentrated on a narrow band from the dominant landslide direction. The directional spreading of waves generated by the deformable landslide is much more significant. In addition, the waves induced by the deformable landslide reach their maximum heights shortly after the release of the sliding mass, and then decay as the sediment spreads and diffuses. While the surface waves which the rigid landslide generates develop slowly. This is more clearly observed by comparing Figs. 23 and 26, which demonstrates the temporal variations of the surface elevation at the centerline transect generated by the rigid landslide. At the early stage of the landslide, the deformable landslide has larger speed and acceleration, resulting in larger surface waves. However, as the rigid landslide continuously accelerates, it can generate larger waves eventually.

The differences of the surface wave features are partly caused by the different kinematics of the rigid and deformable landslides, which are displayed in Fig. 27. The displacement of the rigid landslide is described as Eq. (30), while the along-slope displacement of the deformable landslide is calculated by

$$s_s = \frac{\int_V sCdV}{\int_V CdV} \tag{34}$$

where s_s is the along-slope distance from the initial centroid of the landslide, C is the sediment volume concentration, V is the volume of the landslide, which is identified as the sliding mass with sediment mass concentration greater than 0.01 kg/m^3, dV is the cell volume.

In Fig. 27, the displacements of the centroid (solid line) and leading edge (dash-dotted line) of the deformable landslide are both presented. Due to the spreading of the landslide, these two displacements are different. Apparently, the sliding speed at the leading edge is faster than that at the centroid. It is noticed that, at the early stage of landslide (approximately < 40 s), the speed of the deformable landslide estimated by the gradient of the dash-dotted curve is faster than that of rigid landslide, which leads to larger surface waves. After that, the deformable landslide seems having a constant slide speed. The along-slope displacement is nearly a linear function of time. However, the rigid landslide is still in the acceleration stage till around the characteristic time $t_0 = 78.1$ s, when the landslide reaches its terminal velocity. In order to assess the spreading of the deformable landslide, we define the along-slope and cross-slope spreading distances x_l and y_l as

$$x_l = \frac{\int_V |s - s_c|CdV}{\int_V CdV} \tag{35}$$

$$y_l = \frac{\int_V |y - y_c|CdV}{\int_V CdV} \tag{36}$$

where (s_c, y_c) is the centroid of the landslide. The temporal variations of (x_l, y_l) are presented in the middle panel of Fig. 27, where the solid line denotes the varying x_l, and dashed line represents y_l. As the landslide moves downslope, x_l and y_l both increase, indicating that the landslide is spreading while sliding. The lateral (cross-slope) spreading is much more significant than the along-slope spreading. This can also be found by looking at the temporal variations of the length L and width W of the deformable landslide, which are shown in the third panel of Fig. 27. To determine L and W, the landslide is identified as the sliding mass with sediment concentration greater than 0.01 kg/m^3. The length L is initially two times bigger than the width W. The cross-slope spreading rate is greater so that the length L and the width W are nearly equal at $t = 100$ s. The different spreading rates in the along-slope and cross-slope directions lead to the change of the slide shape, as shown in Fig. 28, which displays the temporal variations of sediment concentration distributions at the bottom layer. The landslide initially has an elliptical shape. However, it becomes more and more circular while moving downslope. The high-concentration landslide is diluted and diffused simultaneously.

5. Conclusions

This paper presents a new submarine landslide model base on the Non-Hydrostatic WAVE model (NHWAVE) (Ma et al., 2012). The model solves free surface elevation directly, which makes it more efficient than VOF and SPH models. The landslide is simulated as water–sediment mixture, which can be diffused and
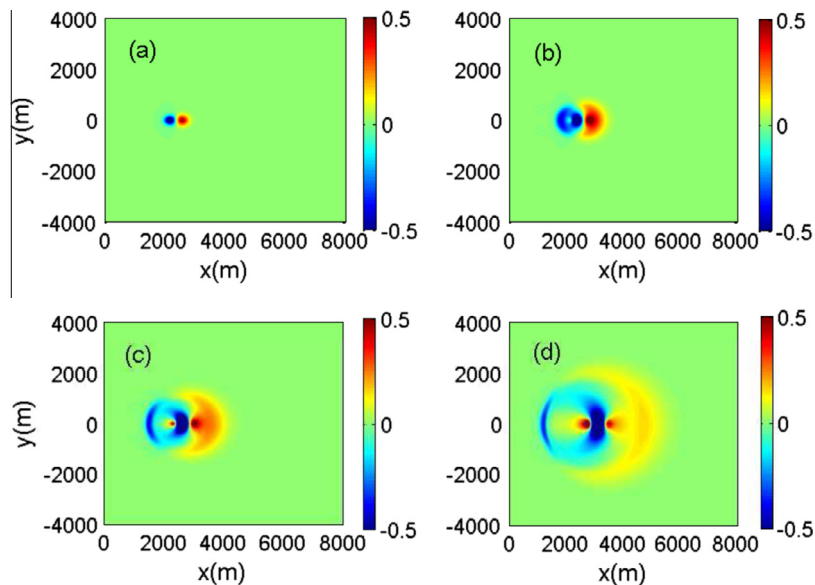
Fig. 25. Snapshots of Tsunami waves generated by a 3D rigid landslide at (a) $t = 10$ s; (b) $t = 30$ s; (c) $t = 50$ s and (d) $t = 80$ s.
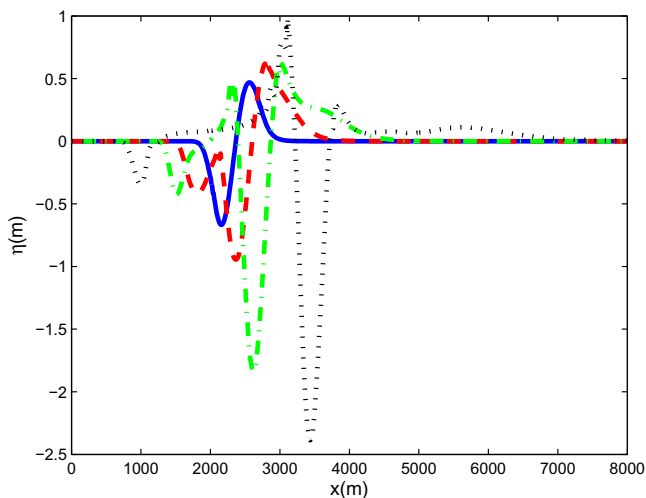

Fig. 26. Free surface elevations in a vertical plane with $y = 0$ m generated by a rigid landslide at $t = 10$ s (solid line); $t = 30$ s (dashed line); $t = 50$ s (dash-dotted line) and $t = 100$s (dotted line).

diluted during its movement. The dense plume is driven by the baroclinic pressure forcing, which is introduced by the spatial density variation. The model is validated by the laboratory measurements on turbidity currents (García, 1993) as well as the tsunami wave generation by a landslide at laboratory scale (Assier-Rzadkiewicz et al., 1997).

The model is then utilized to simulate a large-scale landslide, which is similar to that of Jiang and Leblond (1992). Our study is particularly focused on investigating the effects of different parameters on the landslide motion and associated surface tsunami waves. Specifically, these parameters include sediment settling velocity w_s, initial depth of the landslide d and slide density ρ_{slide}. The results show that the slide motion and water waves generated by the landslide are both sensitive to these parameters. Increasing the sediment settling velocity, the landslide moves fasters, which can generate larger surface waves. For shallower

landslide, the interactions between the slide and surrounding water are stronger, which leads to create larger surface waves. The wave generation process is more efficient if the Froude number is larger. The slide density is the dominant parameter controlling slide motion and associated water waves. The landslide with higher slide density moves faster downslope and can generate larger tsunami waves. Similar to the findings of Jiang and Leblond (1992), three waves trains can be generated during the landslide motion. One is led by a large wave crest, propagating faster than the slide. The second wave train is led by a large wave trough, which is tied to the slide motion. The third wave train is a trough propagating onshore. In contrast to Jiang and Leblond (1992), the wave trains obtained by the current model are very dispersive, which is also captured by a 3D simulation of deformable landslide. The characteristics of the tsunami waves generated by different types of landslide are also examined. The wave energy is mostly concentrated on a narrow band of the dominant slide direction for the waves generated by rigid landslide, while directional spreading is significant for the waves which the deformable landslide generates. Meanwhile, the waves generated by deformable landslide reach their maximum values earlier than those generated by rigid landslide. It is because the kinematics of the rigid and deformable landslides are significantly different. At the early stage of the landslide, the deformable landslide has larger speed and acceleration, resulting in larger surface waves. As the rigid landslide continuously accelerates, it can generate larger waves eventually, which indicates that the rigid landslide may create worse scenario for tsunami hazard assessment.

The results have shown that the current model is capable of reasonably simulating wave generation by submarine landslides. However, at the early stage of the landslide, the slide motion is primarily controlled by the rheology of the material in ways which are not well captured by the present model's use of linear Newtonian viscosity. Extensions to the model to account for non-Newtonian behavior, including intergrannular stresses, will be reported subsequently along with applications on submarine landslides in realistic settings. We should also point out that, although the model formulation does not preclude application to subaerial landslides, this extension of the model needs further investigations and will be discussed at a later time.
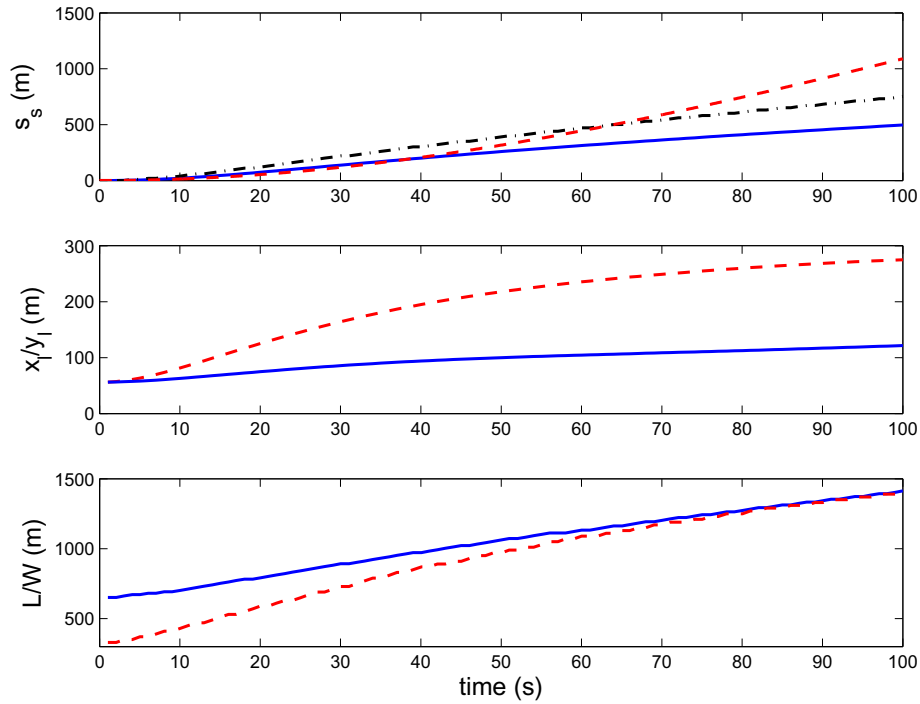
Fig. 27. The along-slope displacement s_s of the deformable (solid line) and rigid (dashed line) landslide (upper panel), the temporal variations of along-slope and cross-slope spreading distances (x_l, y_l) (middle panel) as well as the length L (solid line) and width W (dashed line) of the deformable landslide (lower panel). The displacement of the rigid landslide is described by Eq. (30). The dash-dotted line in the upper panel shows the displacement of the leading edge of the deformable landslide. The landslide is identified as the sliding mass with sediment concentration greater than 0.01 kg/m³.
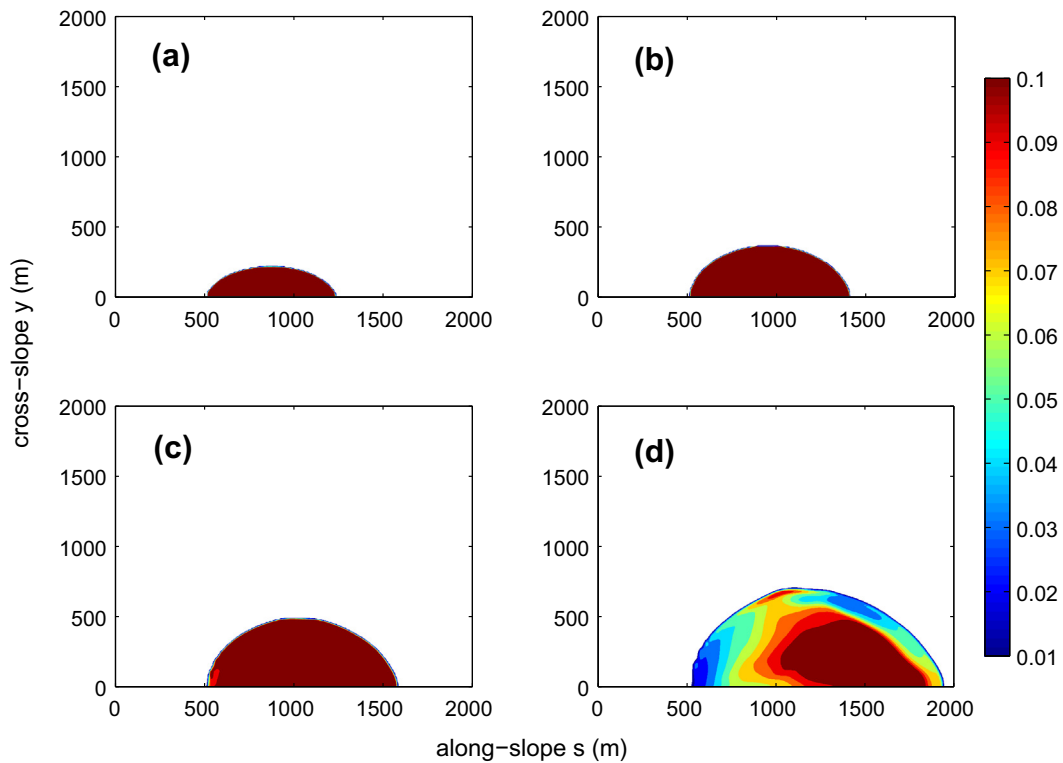

Fig. 28. The movement and spreading of the deformable landslide, which is identified as the sliding mass with sediment concentration greater than 0.01 kg/m³. (a) $t = 10$ s; (b) $t = 30$ s; (c) $t = 50$ s and (d) $t = 100$ s. The distributions of sediment concentration at the bottom layer are demonstrated.

Acknowledgments

References

Abadie, S., Morichon, D., Grilli, S.T., Glockner, S., 2010. Numerical simulation of waves generated by landslides using a multiple-fluid Navier–Stokes model. Coast. Eng. 57, 779–794.

Abadie, S., Harris, J.C., Grilli, S.T., Fabre, R., 2012. Numerical modeling of tsunami waves generated by the flank collapse of the Cumbre Vieja Volcano (La Palma, Canary Islands): Tsunami source and near field effects. J. Geophys. Res. 117, C05030. http://dx.doi.org/10.1029/2011JC007646.

Assier-Rzadkiewicz, S., Mariotti, C., Heinrich, P., 1997. Numerical simulation of submarine landslides and their hydraulic effects, J. Waterway, Port, Coastal, and Ocean Engineering 123, 149–157.

Ataie-Ashtiani, B., Shobeyri, G., 2008. Numerical simulation of landslide impulsive waves by incompressible smoothed particle hydrodynamics. Int. J. Numer. Meth. Fluids 56, 209–232.

Enet, F., Grilli, S.T., 2007. Experimental study of tsunami generation by three-dimensional rigid underwater landslide, J. Waterway, Port, Coastal, Ocean Eng. 133, 442–454.

Fringer, O.B., Gerritsen, M., Street, R.L., 2006. An unstructured-grid, finite-volume, nonhydrostatic, parallel coastal ocean simulator. Ocean Model. 14, 139–173.

Fuhrman, D.R., Madsen, P.A., 2009. Tsunami generation, propagation, and run-up with a high-order Boussinesq model. Coast. Eng. 56, 747–758.

García, M.H., 1993. Hydraulic jumps in sediment-driven bottom currents, J. Hydraul. Eng. 119, 1094–1117.

Giachetti, T., Paris, R., Kelfoun, K., Perez-Torrado, F.J., 2011. Numerical modelling of the tsunami triggered by the Guimar debris avalanche, Tenerife (Canary Islands): Comparison with field-based data. Mar. Geol. 284 (1–4), 189–202.

Gottlieb, S., Shu, C.-W., Tadmor, E., 2001. Strong stability-preserving high-order time discretization methods. SIAM Rev. 43, 89–112.

Grilli, S.T., Watts, P., 1999. Modeling of waves generated by a moving submerged body: Applications to underwater landslides. Eng. Anal. Boundary Elem. 23, 645–656.

Grilli, S.T., Watts, P., 2005. Tsunami generation by submarine mass failure: 1. Modeling, experimental validation, and sensitivity analysis. J. Waterw. Port Coastal Ocean Eng. 131 (6), 283–297.

Grilli, S.T., Vogelmann, S., Watts, P., 2002. Development of a 3D numerical wave tank for modeling tsunami generation by underwater landslides. Eng. Anal. Boundary Elem. 26 (4), 301–313.

Harbitz, C.B., 1992. Model simulations of tsunamis generated by the Storegga slides. Marine Geol. 105, 1–21.

Härtel, C., Meiburg, E., Necker, F., 2000. Analysis and direct numerical simulation of the flow at a gravity-current head. Part 1. Flow topology and front speed for slip and no-slip boundaries. J. Fluid Mech. 418, 189–212.

Harten, A., Lax, P., van Leer, B., 1983. On upstream differencing and Godunov-type schemes for hyperbolic conservation laws. SIAM Rev. 25, 35.

Heinrich, P., 1992. Nonlinear water waves generated by submarine and aerial landslides. J. Waterw. Port Coast. Ocean Eng. 118, 249–266.

Horrillo, J., Wood, A., Kim, G.-B., Parambath, A., 2013. A simplified 3-D Navier–Stokes numerical model for landslide-tsunami: Application to the Gulf of Mexico. J. Geophys. Res. Personal communication.

Imran, J., Harff, P., Park, G., 2001. A numerical model of submarine debris flow with graphical user interface. Comput. Geosci. 27, 717–729.

Jiang, L., Leblond, P.H., 1992. The coupling of a submarine slide and the surface waves which it generates. J. Geophys. Res. 97, 12731–12744.

Jiang, L., Leblond, P.H., 1993. Numerical modeling of an underwater Bingham plastic mudslide and the waves which it generates. J. Geophys. Res. 98, 10303–10317.

Kelfoun, K., Druitt, T.H., 2005. Numerical modelling of the emplacement of Socompa rock avalanche, Chile. J. Geophys. Res. 110, B12202. http://dx.doi.org/10.1029/2005JB003758.

Kelfoun, K., Giachetti, T., Labazuy, P., 2010. Landslide-generated tsunamis at Reunion Island. J. Geophys. Res. 115, F04012. http://dx.doi.org/10.1029/2009JF001381.

Lai, Z., Chen, C., Cowles, G.W., Beardsley, R.C., 2010. A nonhydrostatic version of FVCOM: 1. Validation experiments. J. Geophys. Res. 115, C11010. http://dx.doi.org/10.1029/2009JC005525.

Lin, P., Liu, P.L.-F., 1998a. A numerical study of breaking waves in the surf zone. J. Fluid Mech. 359, 239–264.

Lin, P., Liu, P.L.-F., 1998b. Turbulence transport, vorticity dynamics, and solute mixing under plunging breaking waves in the surf zone. J. Geophys. Res. 103, 15677–15694.

Liu, P.L.-F., Wu, T.-R., Raichlen, F., Synolakis, C.E., Borrero, J.C., 2005. Runup and rundown generated by three-dimensional masses. J. Fluid Mech. 536, 107–144.

Lynett, P., Liu, P.L.-F., 2003. A numerical study of submarine landslide-generated waves and runup. Proc. R. Soc. A 458, 2885–2910.

Ma, G., Shi, F., Kirby, J.T., 2011. A polydisperse two-fluid model for surf zone bubble simulation. J. Geophys. Res. 116, C05010. http://dx.doi.org/10.1029/2010JC006667.

Ma, G., Shi, F., Kirby, J.T., 2012. Shock-capturing non-hydrostatic model for fully dispersive surface wave processes. Ocean Modell. 43–44, 22–35.

Masson, D.G., Harbitz, C.B., Wynn, R.B., Pedersen, G., Lovholt, F., 2006. Submarine landslides: processes, triggers and hazard prediction. Phil. Trans. Roy. Soc. A 364, 2009–2039.

Montagna, F., Bellotti, G., Di Risio, M., 2011. 3D numerical modeling of landslide-generated tsunamis around a conical island. Nat. Hazards 58, 591–608.

Rodi, W., 1987. Examples of calculation methods for flow and mixing in stratified flows. J. Geophys. Res. 92 (5), 5305–5328.

Shi, F., Kirby, J.T., Harris, J.C., Geiman, J.D., Grilli, S.T., 2012. A high-order adaptive time-stepping TVD solver for Boussinesq modeling of breaking waves and coastal inundation. Ocean Model. 43–44, 36–51.

Snyder, P.J., Hsu, T.-J., 2011. A numerical investigation of convective sedimentation. J. Geophys. Res. 116, C09024. http://dx.doi.org/10.1029/2010JC006792.

Synolakis, C.E., Bardet, J.-P., Borrero, J.C., Davies, H.L., Okal, E.A., Silver, E.A., Sweet, S., Tappin, D.R., 2002. The slump origin of the 1998 Papua New Guinea Tsunami. Proc. R. Soc. Lond. Ser. A 458, 763–790.

Tappin, D.R., Watts, P., McMurtry, G.M., Lafoy, Y., Matsumoto, T., 2001. The Sissano, Papua New Guinea tsunami of July 1998 – Offshore evidence on the source mechanism. Mar. Geol. 175, 1–23.

Tappin, D.R., Watts, P., McMurtry, G.M., Lafoy, Y., Matsumoto, T., 2002. Prediction of slump generated tsunamis: The July 17th 1998 Papua New Guinea event. Sci. Tsunami Hazards 20 (4), 222–238.

Toro, E.F., Spruce, M., Speares, W., 1994. Restoration of the contact surface in the HLL-Riemann solver. Shock Waves 4, 25–34.

Torres-Freyermuth, A., Hsu, T.-J., 2010. On the dynamics of wave-mud interaction: A numerical study. J. Geophys. Res. 115, C07014. http://dx.doi.org/10.1029/2009JC005552.

Turner, J.S., 1973. Buoyancy Effects in Fluids. Cambridge University Press, p. 367.

Watts, P., Grilli, S.T., 2003. Underwater landslide shape, motion, deformation, and tsunami generation. In: Proceedings of 13th International Offshore and Polar Engineering Conference, Honolulu, Hawaii, May 25–30.

Watts, P., Grilli, S.T., Kirby, J.T., Fryer, G.J., Tappin, D.R., 2003. Landslide tsunami case studies using a Boussinesq model and a fully nonlinear tsunami generation model. Nat. Hazards Earth Syst. Sci. 3, 391–402.

Yuk, D., Yim, S.C., Liu, P.L.-F., 2006. Numerical modeling of submarine mass-movement generated waves using RANS model. Comput. Geosci. 32 (7), 927–935.

Zhou, H., Teng, M.H., 2010. Extended fourth-order depth-integrated model for water waves and currents generated by submarine landslides. J. Eng. Mech. 136 (4), 506–516.

Zhu, J., 1991. A low-diffusive and oscillation-free convection scheme. Commun. Appl. Numer. Meth. 7, 225–232.